Physics – Uspekhi **68** (2) 146 – 162 (2025)

REVIEWS OF TOPICAL PROBLEMS

PACS numbers: **04.30.–w**, **95.35.+d**, 97.60.Gb

70th ANNIVERSARY OF THE BIRTH OF V.A. RUBAKOV

Precision methods of pulsar timing and polarimetry: results and prospects

K.A. Postnov, N.K. Porayko, M.S. Pshirkov

DOI: https://doi.org/10.3367/UFNe.2024.11.039812

Contents

1. **Introduction** 146
2. **High-precision pulsar timing** 147
   2.1 Brief description of the method; 2.2 Correlations of times of arrival of pulses from different pulsars
3. **Stochastic gravitational wave background in pulsar timing** 149
   3.1 Pulsar Timing Arrays and stochastic gravitational wave background; 3.2 Signal from individual supermassive black hole binaries; 3.3 Astrophysical gravitational wave background; 3.4 Cosmological gravitational wave background
4. **Probing ultralight scalar dark matter using pulsar timing and polarimetry** 154
   4.1 Ultralight pseudoscalar bosons as dark matter; 4.2 Pulsar timing constraints on ultralight scalar dark matter from integral Sachs–Wolfe effect; 4.3 Constraints on ultralight scalar dark matter from pulsar polarimetry
5. **Other applications of pulsar timing** 158
   5.1 Detection of gravitational wave bursts with memory; 5.2 Search for alternative modes of gravitational wave polarization; 5.3 Constraints on graviton mass and GW propagation velocity; 5.4 Study of mass distribution in the Galaxy and search for compact objects
6. **Prospects of pulsar timing method** 160
   References 161

Abstract. **Pulsar timing is a sensitive tool of modern astrophysical research enabling measurements of the time delay of electromagnetic signals propagating from the source to the observer. Modern pulsar timing arrays (PTAs) are used to address various astrophysical problems, including the direct detection of space–time metric perturbations caused, in particular, by gravitational waves. We review the current status of pulsar timing research and recent results on the detection of a stochastic gravitational wave background at nanohertz frequencies of astrophysical and cosmological origin reported by the international collaborations NANOGrav, EPTA, InPTA, PPTA, and CPTA. We also discuss current constraints on scalar ultralight dark matter (pseudoscalar axion-like bosons) posed by the pulsar timing and polarimetry and prospects of these methods to solve other problems of fundamental physics and cosmology.**

K.A. Postnov [1,2,a], **N.K. Porayko** [3,4,b], **M.S. Pshirkov** [1,5,6,c]
(1) Lomonosov Moscow State University, Sternberg State Astronomical Institute, Universitetskii prosp. 13, 119234 Moscow, Russian Federation
(2) Kazan Federal University, ul. Kremlevskaya 18, 420008 Kazan, Russian Federation
(3) Max-Planck-Institut für Radioastronomie, Auf dem Hügel 69, Bonn, 53121, Germany
(4) Università degli Studi di Milano-Bicocca, Piazza dell'Ateneo Nuovo, 1, Milano, 20126, Italy
(5) Institute for Nuclear Research, Russian Academy of Sciences, prosp. 60-letiya Oktyabrya 7a, 117312 Moscow, Russian Federation
(6) Lebedev Physical Institute, Russian Academy of Sciences, Astro Space Center, Pushchino Radio Astronomy Observatory, 142290 Pushchino, Moscow region, Russian Federation
E-mail: (a) director@sai.msu.ru, (b) nporayko@mpifr-bonn.mpg.de, (c) pshirkov@sai.msu.ru

Received 30 October 2024, revised 18 November 2024
Uspekhi Fizicheskikh Nauk **195** (2) 154 – 171 (2025)
Translated by K.A. Postnov

Keywords: radiopulsars, pulsar timing, gravitational waves, stochastic gravitational wave background, supermassive binary black holes, ultralight scalar dark matter

1. Introduction

In this paper, we review the method of pulsar timing (PT), which is a technique for the precise measurement of the times of arrival (ToAs) of pulses from pulsars acting as stable natural cosmic clocks. Pulsar timing is an essential tool in the search for gravitational waves (GWs) from both individual sources and the stochastic GW background (GWB). Two seminal theoretical papers by V.A. Rubakov are of particular relevance in this area of modern experimental astrophysics. He was among the first to calculate the stochastic GWB from the inflationary stage of the expansion of the Universe [1], which is one of the viable targets of the PT experiment. In addition, he proposed a methodology of searching for a monochromatic signal from ultralight scalar dark matter (DM) in the Galaxy using PT data [2].

The search for low-frequency GWs using PT is the concept of detecting distortions of the space–time metric by precisely measuring the ToAs of signals from highly stable periodic sources (natural or artificial 'clocks'). The application of pulsar timing for low-frequency GWs was proposed in the pioneering work of M.V. Sazhin [3] and S. Detweiler [4].[1] Indeed, in the simplest case, the trajectory of a photon with a frequency f in the field of a monochromatic plane-polarized GW and amplitude $h_+ \ll 1$ (for simplicity, only '$+$' polarization is considered) propagating along the z-axis, which is perpendicular to the line of sight (LoS) to the source, residing at distance D, is described by the equation $\mathrm{d}s^2 = 0 = -c^2\,\mathrm{d}t^2 + (1 + h_+(z,t))\,\mathrm{d}x^2 + (1 - h_+(z,t))\,\mathrm{d}y^2 + \mathrm{d}z^2$.

The travel time of such a signal from the source to the observer along the x-axis will change by the amount

$$\delta t = \frac{D}{c}\left[\left(1 \pm \frac{1}{2}\,h_+(t)\right) - \left(1 \pm \frac{1}{2}\,h_+\left(t - \frac{D}{c}\right)\right)\right]$$
$$= \pm\frac{D}{2c}\left(h_+(t) - h_+\left(t - \frac{D}{c}\right)\right),$$

which corresponds to the shift in the frequency of the received signal[2] $\Delta f(t)/f = (1/2)(h_+(t) - h_+(t - D/c))$. Delays in a ToA of periodic pulses accumulated during the observation time T are

$$\mathcal{R}(T) = \int_0^T \frac{\Delta f(t)}{f}\,\mathrm{d}t\,.$$

In the general case, a plane GW with frequency $f = \omega/2\pi$, dimensionless amplitude h_c, and polarization angle ϕ propagating at an angle θ to the LoS of a pulsar will cause sinusoidal oscillations in the ToAs of its pulses with characteristic amplitude [8, 9]

$$\Delta t = \frac{h_\mathrm{c}}{\omega}\,[1 + \cos\theta]\sin(2\phi)\sin\frac{\omega D[1 - \cos\theta]}{2c}\,, \qquad (1)$$

where c is the speed of light (below, unless specified, we use the natural system of units $\hbar = c = k_\mathrm{B} = 1$).

The largest magnitude of the effect is achieved for a total observing time of the order of $T = 1/f$. For a characteristic timespan of observations of several years ($T \sim 10^8$ s), the amplitude of the ToA variations will be of the order of $\mathcal{A} = h_\mathrm{c}/\omega \sim 20$ ns for $h_\mathrm{c} \sim 10^{-15}$. After subtracting the known deterministic contributions encapsulated in the pulsar timing model due to the motion of the observatory in the gravitational field of the Sun and planets in the Solar system and taking into account the orbital motion of a pulsar in a binary system, as well as removing the effects of General Relativity (GR) (Römer delay, gravitational redshift, Shapiro delay), clean ToA residuals (also known as post-fit residuals) can be obtained. Post-fit residuals with a typical root-mean-square (RMS) of several dozen ns can be used to search for various effects related to fluctuations of the space–time metric, including GWs from individual supermassive black hole binaries (SMBHBs), stochastic GWB of an astrophysical and cosmological nature, as well as some forms of DM (in particular, ultralight scalar DM causing oscillations of the gravitational potential, considered for the first time by A. Khmelnitsky and V. Rubakov [2]). A detailed review of the astrophysical and cosmological sources of nHz GWs, which the PT method is most sensitive to, can be found in [10]. The present review focuses on these and other possible sources of space–time nonstationarities currently studied with PT.

The structure of the review is as follows. Section 2 briefly presents the essence of the PT method. Section 3 discusses the stochastic GWB and summarizes the results on its detection and interpretation by international PT collaborations. Section 4 is devoted to probes of possible traces of ultralight scalar DM in PT (Section 4.2) and pulsar polarimetry (Section 4.3). Section 5 discusses other possible applications of PT, i.e., the detection of GW bursts with memory, searches for additional modes of GW polarization, constraints on the graviton mass and GW propagation velocity, study of mass distribution in the Galaxy, and the search for compact objects. In conclusion (Section 6), the main trends in the advancement of the PT method in solving astrophysical and cosmological problems are briefly described.

2. High-precision pulsar timing

2.1 Brief description of the method

PT can undoubtedly be called a unique instrument for detecting GWs in the nHz frequency range. Pulsars are rapidly rotating strongly magnetized neutron stars. In the PT context, these cosmic flywheels act as ultrastable clocks located at Galactic distances. However, prior to using pulsars as stable clocks, a number of reductions are necessary, which we describe below.

Individual pulses from pulsars vary considerably in shape and amplitude, but their mean profiles, obtained by averaging a large number (in the case of millisecond pulsars (MSPs), we are talking about $\mathcal{O}(10^6)$ individual pulses), are extremely temporally stable and are a kind of pulsar 'business card'. During a single observing session, the signal is accumulated for a relatively long time (from minutes to tens of minutes), then the signal is folded with a period equal to the spin period of the pulsar at that epoch. The resultant folded profile is then cross-correlated with the mean template profile. The outcome of an individual observational session is a ToA, which typically refers to the time stamp closest to the middle of the session. The accuracy of the measured ToA is approximately determined by W/SNR, where W is the pulse width (not to be confused with the pulsar period P) and SNR is the signal-to-noise ratio (SNR) of the observed profile [11]:

$$\mathrm{SNR} \propto S_\mathrm{psr}\sqrt{t_\mathrm{obs}\Delta f}\sqrt{\frac{P}{W}}\,, \qquad (2)$$

where S_psr is the mean flux density of the pulsar, t_obs is the total duration of the session, and Δf is the instrument bandwidth. It is clear that SNR is larger for bright pulsars with sharp profile shapes (so that the W/P ratio is smaller) observed over a longer period of time in a wider frequency bandwidth. In absolute values, the RMS error of the

[1] See also earlier study [5], where the authors calculated the GW-induced variation in a frequency of a periodic signal received on Earth during Doppler tracking of a spacecraft.

[2] The expression for the redshift of the observed frequency in the GW field can be derived in a straightforward way from the Sachs–Wolfe formula, originally used to describe the fluctuations in the temperature maps of the cosmic microwave background (CMB) [6, 7]:

$$\frac{\Delta T}{T} = -\frac{1}{2}\int_{\lambda_\mathrm{e}}^{\lambda_\mathrm{o}} \frac{\partial h_{ij}}{\partial t}\,\hat{n}_i\hat{n}_j\,\mathrm{d}\lambda$$

($\hat{n}_i$, $\hat{n}_j$ is the unit vector in the pulsar direction; the integral is taken along the photon path).

determined ToA $\sigma_{\rm TOA} = (\langle \mathcal{R}^2(t)\rangle)^{1/2}$ is smaller for MSPs, which, together with their high rotational stability, explains their usefulness in searches for GW and other physical effects considered in this review.

Due to gradual loss of the pulsar's rotational energy, its spin frequency ν slowly decreases [12]. This spin-down can be described as follows:

$$\nu(t) = \nu(t_0) + \dot{\nu}_0(t - t_0) + \frac{1}{2}\,\ddot{\nu}_0(t - t_0)^2 + \ldots \qquad (3)$$

(hereafter, the subscript 0 denotes the value at time t_0, e.g., $\nu_0 \equiv \nu(t_0)$).

One can easily obtain the value of the pulsar rotational phase at any given time t relative to the initial moment t_0:

$$N(t) = N_0 + \int_{t_0}^{t} \nu(t)\,\mathrm{d}t = N_0 + \nu_0(t - t_0) + \frac{1}{2}\,\dot{\nu}_0(t - t_0)^2 + \frac{1}{6}\,\ddot{\nu}_0(t - t_0)^3 + \ldots\,. \qquad (4)$$

This relation holds true in the pulsar reference frame. To convert it to the reference frame of a ground-based observatory, the appropriate reduction must be made.

For relation (4) to remain valid, it is necessary to use a time scale associated with a reference frame that is as close as possible to the inertial one. At present, such a reference frame is a barycentric coordinate system, with the origin in the barycenter of the Solar system, and the corresponding Barycentric Coordinate Time (TCB, Temps-Coordonnée Barycentrique).

We will consider an isolated single pulsar and assume that it is at rest with respect to the chosen reference frame. A uniform motion will not change the form of (4), but will only redefine the observed value of the pulsar spin frequency compared to its intrinsic value due to the Doppler shift. First, ToAs at the observatory are calculated w.r.t a local timescale defined by the local hydrogen standard. Further reduction is carried out in a series of steps. First, using global navigation satellite systems such as GPS or GLONASS, the local time scale is connected to the Coordinated Universal Time (UTC) rigidly linked to the International Atomic Time (TAI) scale, which is a weighted average of several hundred atomic clocks at various national laboratories. The next step is a reduction to the most stable Terrestrial Time (TT) scale, which is the closest possible approximation to an ideal uniform atomic clock at the level of the local geoid.

Finally, the ToAs of the pulse received at the telescope are recalculated to the barycenter of the Solar system. In this process, high-precision ephemerides are used, such as those developed by the NASA Jet Propulsion Laboratory (JPL NASA) DE440, or IPA RAS EPM2021. In addition to the Römer delay between the telescope and the Solar system barycenter, relativistic effects, such as the Shapiro delay and the effect of time dilation on the moving Earth and in the gravitational fields of Solar system bodies, are taken into account [13, 14]. Currently, the accuracy with which we can account for all of these effects is about 100 ns, which is equivalent to knowing the position of the barycenter with a precision of up to tens of meters. Even such small uncertainties can bias the detection of GWs with PT [15].

The ToA obtained in the TCB is the main result of this reduction. This procedure of ToA extraction is carried out over many years with a cadence of several weeks, forming a long-time series of ToAs. The most up-to-date PT ephemerides are obtained using the least-squares fit of the PT model to this ToA time series:

$$\chi^2 = \sum_i \left(\frac{N(t_i) - n_i}{\sigma_i}\right)^2, \qquad (5)$$

where $N(t_i)$ is the pulse number corresponding to the ToA t_i; n_i is the integer number closest to $N(t_i)$, since, for an ideal model between each pair of ToAs, an integer number of rotations of the pulsar must have occurred; and σ_i is the measurement error of the ith ToA in units of pulsar period. Given that there are a number of effects that are not accounted for by the pulsar timing model, $N(t_i) \neq n_i$, and ToA residuals are nonzero, $\mathcal{R} \equiv P(N(t_i) - n_i)$. In practice, this least-square fit is routinely performed using TEMPO and TEMPO2 [3] software packages [16, 17].

If the PT model ephemerides have been correctly determined, i.e., when they are close to their true values, the residuals behave like 'white noise' with the RMS close to the ToA uncertainty in individual sessions $\sigma_{\rm TOA}$. If there is an error in the parameter values, the residuals display a characteristic structure that enables one to refine the ephemeris. For example, sinusoidal oscillations with an annual period would indicate incorrect determination of the celestial coordinates of the pulsar that lead to a wrong estimation of the Römer delay and errors in the reduction to the barycenter of the Solar system. That is, PT is an iterative tool for fitting and refining the PT model parameters when new data are added at each consecutive step.

The presence of a GWB will give rise to 'red noise' [4] in the residuals. It should be noted that residuals with similar spectral properties can also be induced by other astrophysical processes, such as irregularities in pulsar rotation (pulsar intrinsic 'red noise'), noise in the atomic time standards which are used to measure ToAs at the observatory, and turbulence of the interstellar medium. For instance, the last causes a stochastic signal in the residuals with the amplitude depending on the observing frequency. The main difficulty in the GWB detection using the PT method lies in separating the sought signal from other aforementioned stochastic contributions. The nontrivial spatial correlation of the GW signal, which will be discussed in Section 2.2, greatly simplifies this task.

2.2 Correlations of times of arrival of pulses from different pulsars

The quadrupole nature of GWs leads to a unique correlation in the ToAs of pulsars that depends on the angular separation between the pulsars in pairs. If there is an isotropic stochastic GWB with equal power in all directions, the correlation of the ToA residuals from a pair of pulsars with an angular separation γ_{ij} between them is described by the so-called Hellings–Downs (HD) curve [18]:

$$\alpha_{ij} = \frac{1}{4\pi}\int \alpha_i \alpha_j\,\mathrm{d}\Omega = \frac{1 - \cos\gamma_{ij}}{2}\ln\left(\frac{1 - \cos\gamma_{ij}}{2}\right) - \frac{1}{6}\,\frac{1 - \cos\gamma_{ij}}{2} + \frac{1}{3} \qquad (6)$$

(see [19] for the detailed derivation and discussion of limitations of this formula).

[3] https://sourceforge.net/projects/tempo2/.

[4] The power spectral density increases with decreasing frequency.

The effect of GWs on pulsar ToAs includes two contributions, the 'Earth term' and the 'pulsar term,' which correspond to the metric perturbation on Earth and at the pulsar, respectively. Since distances to pulsars are poorly known, it is usually possible to correlate only the common 'Earth' part. This leads to a 'blurring' of the HD dependence (known as HD variance). Adding pulsar distances as free parameters in the analysis can lead to an increase in the SNR of the GW signal from an individual SMBHB and a more accurate estimation of the distance to this source [20]. For a stochastic GWB, as shown in [21], the pulsar variance of the HD curve can be suppressed by increasing the number of observed pulsars and then averaging over multiple pulsar pairs over some range of angular distances γ_{ij}.

Another effect that leads to scattering of the expected HD curve is related to so-called cosmological variance [21–23]. Cosmological variance is caused by the interference of several GW sources emitting at the same frequency, which leads to a deviation from the canonical curve. The specific form of the modified HD curve will depend on the realization of an ensemble of SMBHBs in the observed Universe. Unlike the pulsar variance, cosmological variance cannot be suppressed by increasing the number of pulsars in the analysis.

3. Stochastic gravitational wave background in pulsar timing

A stochastic GWB is generated by a population of independent sources of GWs $h_{ij}(\mathbf{x}, t)$, and is treated as a random variable over an ensemble of realizations. It is conveniently described by the dimensionless spectral amplitude $h_c(k, t)$, which, for a homogeneous and isotropic unpolarized random Gaussian background, is

$$\langle h_l(\mathbf{k}, t) h_m(\mathbf{q}, t)\rangle = \frac{8\pi^5}{k^3}\,\delta^3(\mathbf{k}-\mathbf{q})\delta_{lm}\, h_c^2(k, t)\,, \tag{7}$$

where $k = |\mathbf{k}|$. Given this definition, the relation with the random tensor amplitudes of the metrics of two polarizations is given by the expression

$$\langle h_{ij}(\mathbf{x}, t) h_{ij}(\mathbf{x}, t)\rangle = 2\int_0^\infty \frac{dk}{k}\, h_c^2(k, t)\,. \tag{8}$$

It can be shown that $h_c(k, t)$ is the characteristic amplitude of the metric in the logarithmic interval of wavenumbers per polarization. A common practice is to introduce the power spectrum $P_h(k, t) \equiv 2h_c^2(k, t)$. The energy density of the GWB is

$$\rho_{\rm GW} = \int \frac{dk}{k}\frac{d\rho_{\rm GW}}{d\log k} = \frac{\langle \dot{h}_{ij}(\mathbf{x}, t)\dot{h}_{ij}(\mathbf{x}, t)\rangle}{32\pi G}\,. \tag{9}$$

To relate to observed quantities, one can introduce a one-sided GWB spectral density $S_h(f)$ [Hz^{-1}] in terms of frequency $f = k/(2\pi)$,

$$S_h(f) = \frac{h_c^2(f)}{2f}\,, \tag{10}$$

which is convenient to relate to the noise power spectral density of a receiver $S_{\rm n}(f)$.

The GWB (especially of a cosmological nature) is conventionally characterized in terms of the dimensionless ratio of the GW energy density per logarithmic frequency interval to the critical density of the Universe, $\rho_c = 3H_0^2/(8\pi G)$ (where H_0 is the present value of the Hubble parameter):

$$\Omega_{\rm GW}(f) = \frac{4\pi^2}{3H_0^2}\, f^3 S_h(f) = \frac{2\pi^2}{3H_0^2}\, f^2 h_c^2(f)\,. \tag{11}$$

In terms of the dimensionless amplitude of metric $h_c = \sqrt{2fS_h}$,

$$S_h(f) \approx 8\times 10^{-37}[\mathrm{Hz}^{-1}]\left(\frac{\mathrm{Hz}}{f}\right)^3\left(\frac{H_0}{100\ \mathrm{km\ s^{-1}\ Mpc^{-1}}}\right)^2\Omega_{\rm GW}(f)\,, \tag{12}$$

$$h_c \approx 1.26\times 10^{-18}\left(\frac{\mathrm{Hz}}{f}\right)\left(\frac{H_0}{100\ km\ \mathrm{s^{-1}\ Mpc^{-1}}}\right)\sqrt{\Omega_{\rm GW}(f)}\,. \tag{13}$$

When searching for the stochastic GWB with PT, we use the power spectral density of the correlated residuals [24]. In this case, instead of the GWB spectral density $S_h(f)$, we use the one-sided spectral density of the residuals[5] $S_n(f)$ with dimensionality Hz^{-3}:

$$S_n(f) = \frac{1}{12\pi^2}\frac{h_c^2(f)}{f^3}\,. \tag{14}$$

After substituting the relation of $h_c^2(f)$ with $\Omega_{\rm GW}(f)$ from (11), we obtain

$$S_n(f) = \frac{H_0^2}{8\pi^4}\frac{\Omega_{\rm GW}(f)}{f^5}\,. \tag{15}$$

The RMS of the induced residuals with a total time span T in the frequency bins $\Delta f_i = 1/T$ are related to the spectral density $S_n(f)$:

$$\sigma_{{\rm TOA},\,i} = \left(\int_{\Delta f_i} S_n(f)\,df\right)^{1/2} \approx \left(S_n(f_i)\Delta f_i\right)^{1/2} = \left(\frac{S_n(f_i)}{T}\right)^{1/2}. \tag{16}$$

For characteristic values T and h_c, we obtain

$$\begin{aligned}\sigma_{\rm TOA} &\approx 1.6\times 10^{-8}[\mathrm{s}]\left(\frac{h_c}{10^{-15}}\right)\left(\frac{f}{10^{-8}\ \mathrm{Hz}}\right)^{-3/2}\left(\frac{T}{1\ \mathrm{year}}\right)^{-1/2}\\ &\approx 2\times 10^{-8}[\mathrm{s}]\left(\frac{f}{10^{-8}\ \mathrm{Hz}}\right)^{-5/2}\left(\frac{H_0}{100\ \mathrm{km\ s^{-1}\ Mpc^{-1}}}\right)\\ &\quad\times\left(\frac{\Omega_{\rm GW}}{10^{-10}}\right)^{1/2}\left(\frac{T}{1\ \mathrm{year}}\right)^{-1/2}.\end{aligned} \tag{17}$$

The signal generated by the GWB is demonstrated in Fig. 1b. ToA residuals with RMS of tens of ns are potentially measurable by present-level PT experiments.

For the characteristic amplitude h_c, a power-law parametrization is often used:

$$h_c(f) = A\left(\frac{f}{f_0}\right)^\alpha\,, \tag{18}$$

[5] The extra square of frequency in the denominator of the residual power spectrum appears because the RMS of the residuals is expressed as

$$\langle \mathcal{R}^2(t)\rangle = \int_0^\infty \frac{1}{3}\frac{h_c^2(k)}{k^2}\frac{dk}{k} = \int_0^\infty df\, S_n(f)$$

(the factor $1/3$ arises when averaging over the distances to the pulsars under the condition $\omega D \gg 1$). Since the residuals are in [s], the power spectrum $S_n(f)$ has the dimension [$\mathrm{s}^2\ \mathrm{Hz}^{-1}$] = [$\mathrm{Hz}^{-3}$].

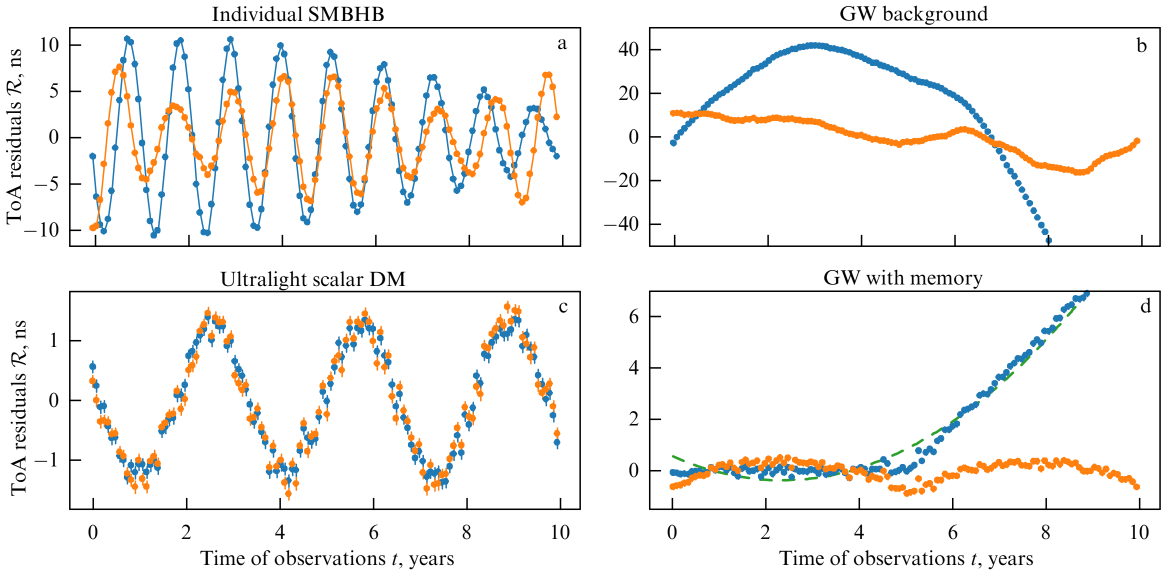

Figure 1. From left to right and from top to bottom: (a) Model residuals from an individual SMBHB with chirp mass equal to $10^9 M_\odot$ and orbital frequency $f = 10^{-8}$ Hz located at distance $D_L = 10$ Mpc; orange curve shows that the signal contains two frequency harmonics corresponding to short-period Earth and long-period pulsar terms; (b) model signal from stochastic GWB with $h = 10^{-15}$ and $\alpha = 2/3$; (c) model signal due to Sachs–Wolfe effect from ULDM with $m_a = 5 \times 10^{-23}$ eV; (d) expected residuals from a burst with memory with $h_{\rm mem} = 5 \times 10^{-16}$ and burst epoch $t_B = 5$ years. For all simulations, total duration of observations is 10 years. Original signal is shown in blue, and signal after subtracting quadratic fitting function is shown in orange. Green line in (iv) shows fitting function.

where the reference frequency is usually set to $f_0 = 1$ year^{-1}. Then, the relation of the signal power spectrum in the residuals caused by a stochastic GWB with the amplitude A and the spectral index α is given by (substituting (18) into (14))

$$S_n(f) = \frac{A^2}{12\pi^2 f_0^{2\alpha}} f^{-\gamma}, \quad \gamma = 3 - 2\alpha. \tag{19}$$

Such a model arises both in the classical astrophysical model and in many cosmological scenarios. At least such a parametrization is a sufficiently valid approximation for small SNR regimes (see the explanation in the following sections).

3.1 Pulsar Timing Arrays and stochastic gravitational wave background

Pulsar Timing Arrays (PTAs) are primarily designed to detect stochastic GWB signals and long-period signals from individual sources, such as merging SMBHBs. The sought signal is not transient, but stays in the frequency window of the PT sensitivity with a width $\Delta f \sim 1/T$ for a substantial time. Thus, there is an accumulation effect: an increase in the total time span of observations T in combination with the ever-increasing sensitivity of radio telescopes will inevitably increase the SNR and the significance of the detection.

For a PTA observing N identical pulsars over time T with sampling period Δt and ToA error $\sigma_{\rm TOA}$, the SNR of the GWB will grow with amplitude A as

$$\mathrm{SNR} \propto \sqrt{N_{\rm psr}(N_{\rm psr}+1)}\, \frac{\Delta t^a A^b T^c}{\sigma^d_{\rm TOA}},$$

where the values a, b, c, d depend on the SNR regime we are working in (see [25, 26]). In the weak signal regime (when the spectrum of the GWB lies below the level of instrumental noise over the entire frequency range), $a = -1$, $b = 2$, $c = 3 - 2\alpha$, and $d = 2$. In the case of intermediate sensitivity, when for at least one frequency bin the spectral power of the signal lies above the noise, the parameters are $a = 1/(6 - 4\alpha)$, $b = 1/(3 - 2\alpha)$, $c = 1/2$, and $d = 1/(3 - 2\alpha)$. When deriving these expressions, we used a simple model of the power spectral density of metric fluctuations $S_h(f) \sim f^{2\alpha-1}$ corresponding to the power-law parametrization of $h_c(f)$ (18).

We would like to emphasize that the equations are derived specifically for the SNR of the HD correlation (not the SNR of the uncorrelated stochastic signal common to all pulsars), i.e., only the cross-correlated terms were included in the estimates. When taking into account the auto-correlation terms, the SNR will grow as $\sim \sqrt{N_{\rm psr}}$ [27]. The expressions above show that PT is aimed at detecting GWs from the initial long-lasting stages of merging of binaries (the 'inspiraling' stage). In this case, the SNR increases as the data are accumulated. It is opposite to the case of ground-based GW laser interferometers, which are designed to detect transient GW signals from the last stages of coalescence of compact binary black holes and neutron stars which sweep the detector sensitivity band only for several seconds.

In 2023, the major PTA Collaborations, the North American NANOGrav [28], the European EPTA and Indian InPTA [29], the Australian PPTA [30], and the Chinese CPTA [31], independently reported the detection of a stochastic signal (red noise) at nHz frequencies, which evidences HD correlation for different pulsar pairs and is therefore most likely of GW origin. See Table 1 for the essential characteristics of the aforementioned PTAs: the number of pulsars, the duration of observations, and the observing frequency bands. The analysis was performed within the framework of frequentist and Bayesian statistics [32]. The significance of the HD angular correlation found ranges from 2σ to 4.6σ and is highly dependent on the chosen dataset and the processing pipeline. In Fig. 2, we present the results of the search for angular correlations of the PT residuals independently published by international PTAs. The spectral characteris-

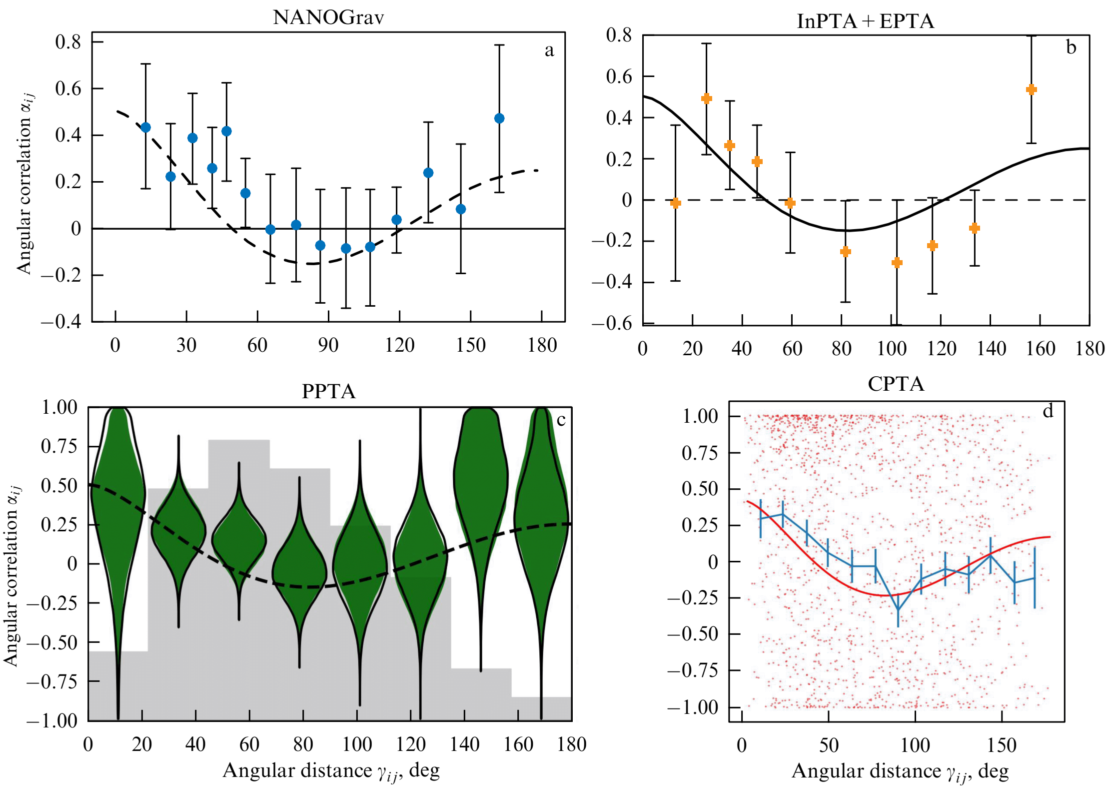

Figure 2. Angular correlation α_{ij} averaged for many pulsar pairs as a function of angular distance between pulsars γ_{ij} obtained by different PTAs (left-to-right, top-to-bottom): NANOGrav, EPTA (DR2New), PPTA, CPTA. Theoretically expected curve is shown by dashed (NANOGrav and PPTA), solid (EPTA and CPTA) lines, respectively. For NANOGrav, EPTA, PPTA, the sought signal is a stochastic process with a spectrum described by a power-law function. For CPTA, a monochromatic signal was searched for in three lowest frequency windows. Graph shows resulting angular correlation for one of them, $f = 1.5/T$, where T is total CPTA observation time. Additionally, correlations of individual pulsar pairs are marked with red dots. (From papers [28–31].)

Table 1. Amplitude of astrophysical stochastic GW background at $f_0 = 1$ year^{-1} with slope $\alpha = -2/3$ from observations of various PTAs. For EPTA, results of analyzing latest 10-year data segment (EPTA DR2New) are shown. InPTA data are available for only 10 of 25 pulsars observed by EPTA.

Network	Duration, years	Number of pulsars $N_{\rm psr}$	Frequency, MHz	Amplitude $A/10^{-15}$ * ($f = 10^{-7}-10^{-9}$ Hz)	Literature
NANOGrav	15	67	327 – 3000	$2.4^{+0.7}_{-0.6}$	[33]
EPTA/InPTA	10.3/25	25	300 – 4857	2.5 ± 0.7	[34]
PPTA	18	30	692 – 4032	$2.04^{+0.25}_{-0.22}$	[30]
CPTA	3.5	57	1250	2^{+8}_{-80}	[31]

* For $f_0 = 1$ yr^{-1}, isotropic GWB from coalescing SMBHs $\gamma = 13/3$.

tics of the signal found by different PTAs, assuming a theoretically motivated slope of the power spectrum of residuals $\gamma = 13/3$ ($\alpha = -2/3$), are summarized in Table 1. Properties and a possible interpretation of the detected signal are discussed in more detail in the next section.

3.2 Signal from individual supermassive black hole binaries

The most expected GW sources in the range of PT sensitivity are SMBHBs, which are assumed to form in the centers of galaxies in the aftermath of the merger process during hierarchical assembling of galaxies [35]. The metric perturbation from such a binary is represented by a monochromatic wave with frequency $f_{\rm GW}$ twice the orbital one (for circular orbits). The response of a PTA to such a signal includes the Earth and pulsar terms describing the metric perturbations near Earth at time t and near the pulsar at time $t - \tau_{\rm a}$, respectively [36]:

$$\mathcal{R}(t) = \sum F^A(\hat{\Omega})\left[\mathcal{R}_A(t) - \mathcal{R}_A(t-\tau_{\rm a})\right], \qquad (20)$$

where $F^A(\hat{\Omega})$ is the antenna pattern of the PTA which describes how each of the GW polarizations ($+, \times$) perturbs the residuals, depending on the source direction $\hat{\Omega}$, $\tau_{\rm a} = D/c$. The amplitude of the signal in the residuals is determined by the chirp mass of the binary $\mathcal{M} = (M_1 M_2)^{3/5}/(M_1 + M_2)^{1/5}$ and the photometric distance to the source d_L[6]:

$$\mathcal{A} \equiv \frac{h_{\rm c}}{2\pi f_{\rm GW}} = \frac{\mathcal{M}^{5/3}}{d_L(\pi f_{\rm GW})^{1/3}}\,. \qquad (21)$$

[6] The dimensionless amplitude of metric perturbations from the binary is $h = 2\mathcal{M}^{5/3}(\pi f_{\rm GW})^{2/3}/d_L$.

The full expression for $\mathcal{R}_A(t)$ depends on the GW polarization angle, the orbital phase, and the orbital inclination angle of the binary (see formula (1)) and is given in [37]. A signal from an individual SMBHB with characteristic parameters is shown in Fig. 1a.

The signal from an individual source will also have the spatial correlation described by the HD curve. Therefore, at low SNRs, the stochastic GWB and the deterministic signal from an SMBHB in the PT data will be strongly covariant, which was confirmed by simulations in [37]. Indeed, as independently shown in [38] and [37], the detected signal can be described by a monochromatic GW with a frequency of ~ 4 nHz. Assuming that the binary system is at a distance of 10 Mpc (slightly less than the characteristic distance to the galaxy clusters in Fornax and Virgo), the chirp mass of the merging binary is $\mathcal{M} \simeq 10^9 M_\odot$.

In addition to blind searches, in which there is no prior knowledge of the binary's sky coordinates, there are also targeted searches for GW signals from candidates based on electromagnetic (EM) surveys [39, 40]. This enables increasing the sensitivity locally for specific regions of the sky.

3.3 Astrophysical gravitational wave background

As shown in [41] using realistic simulations, the detection probability of a stochastic GWB, which is an incoherent sum of signals from the whole population of SMBHBs, is ~ 5 times greater than the probability of detecting a deterministic signal from an individual source. Thus, the stochastic GWB is the most promising signal to be probed by PTAs.

The stochastic GWB from the population of incoherent sources of the same nature in the isotropic and homogeneous Universe can be easily calculated analytically [42]. Given the source number density $n(z)$, the contribution to the GWB at frequency f will be determined only by the GW energy emitted by a single source in the logarithmic frequency interval $f\,\mathrm{d}E_{\mathrm{GW}}/\mathrm{d}f$ in the source's rest frame at redshift z:

$$\rho_{\mathrm{GW}}(f) \equiv \Omega_{\mathrm{GW}}\rho_{\mathrm{c}} = \int n(z)\,\mathrm{d}z \int \frac{\mathrm{d}E_{\mathrm{GW}}}{\mathrm{d}f'}\,\frac{\mathrm{d}f'}{1+z}$$
$$= \int n(z)\,\mathrm{d}z \int \left(\frac{\mathrm{d}E_{\mathrm{GW}}}{\mathrm{d}\log f'}\right)\frac{\mathrm{d}\log f}{1+z} \tag{22}$$

(the factor $1+z$ in the denominator takes into account the cosmological redshift $f = f'/(1+z)$).

In the case of SMBHBs in circular orbits merging solely due to GW emission (ignoring possible additional factors responsible for the orbital momentum loss), the GW energy radiated at the double orbital frequency in the logarithmic frequency interval is $\mathrm{d}E_{\mathrm{GW}}/\mathrm{d}\log f' = (\pi G f')^{2/3}\mathcal{M}^{5/3}/3$. Substituting this formula into (22), from (11) we find that the amplitude of the signal is determined by the chirp mass of the binary $\mathcal{M}$ and the comoving number density of merging SMBHBs $\mathrm{d}^2 n/\mathrm{d}z\,\mathrm{d}\mathcal{M}$:

$$h_{\mathrm{c}}^2(f) = \frac{4G^{5/3}}{3\pi^{1/3}c^2}\,f^{-4/3}\int \mathcal{M}\int \mathrm{d}z\,(1+z)^{-1/3}\mathcal{M}^{5/3}\,\frac{\mathrm{d}^2 n}{\mathrm{d}z\,\mathrm{d}\mathcal{M}}\,, \tag{23}$$

where z is the redshift. In this case, $h_{\mathrm{c}} \sim (f/f_{\mathrm{ref}})^{-2/3}$ (the slope of the spectrum is $\alpha = -2/3$).

This dependence has a clear physical meaning: for a system in a circular orbit, the dimensionless amplitude of the metric is $h \sim \mathcal{M}^{5/3}\omega^{2/3}/d_L$, and the rate of change of the orbital frequency due to GW radiation is $\dot{\omega} \sim \omega^{11/3}$. Consequently, in the interval of GW frequencies $\Delta f \sim f$, there will be simultaneously $N = f\,\mathrm{d}N/\mathrm{d}f = R\omega/\dot{\omega}$ sources, where R is the merger rate of the binary systems giving the maximum GW amplitude (in this case SMBHBs). Since the sources are evolving independently, the total stochastic signal will have a characteristic amplitude $h_{\mathrm{c}} = \sqrt{N}h \sim f^{-2/3}$.

In reality, the GW spectrum has a more complex structure, and a number of additional factors must be taken into account for its calculation [33, 41]. The nonzero eccentricities of binary systems will lead to a redistribution of the power spectral density from lower to higher GW frequencies. Similarly, the interaction of the binary components and the surrounding gas and stars will result in a loss of power at low GW frequencies. Both phenomena will effectively flatten GW spectra. A finite number of merging binaries will lead to so-called shot-noise of the brightest isolated SMBHBs dominating the overall stochastic signal, which will, on the contrary, effectively increase the slope of the GWB spectrum.

The results obtained by different PTAs (see Fig. 2 and Table 1) are in general agreement with the astrophysical interpretation [33, 34]. Nevertheless, a number of parameters of the astrophysical GWB model are at the borders of their prior distributions. Namely, the spectrum slopes obtained by all PTAs are marginally higher than the predicted $\alpha = 2/3$. Moreover, using semi-analytical numerical modeling, such as L-Galaxies [34, 43], it was shown that, in order to reproduce the found amplitudes of the GWB, it is necessary to significantly increase the mass of the merging components, which can be achieved by increasing the accretion rate onto the black holes. This causes an increase in the luminosity function of quasars, which leads to a contradiction with observations [44].

It should be noted that the results presented in this section were obtained under the simplest assumptions about the properties of the GWB: Gaussianity, isotropy, and a power-law shape of the spectrum. Strictly speaking, these conditions are not fulfilled for the astrophysical GWB. Nevertheless, as shown in [45] using realistic models that take into account the finite number of SMBHBs, the methods of PT analysis within the framework of standard assumptions are able to solve the problem, albeit with a rather significant scatter of the obtained parameters of the GWB and signal significance.

3.4 Cosmological gravitational wave background

The cosmological GWB (CGWB) is probably one of the most interesting targets from the point of view of PT, as it carries unique information about the physical processes that occurred in the very first epochs of the evolution of the Universe (inflation, reheating phase, phase transitions, etc.; see also [10, 46–49] and references therein). Given that gravitational interaction is extremely weak, GWs leave thermodynamic equilibrium with other components of the Universe immediately after their generation. Qualitatively, we can obtain the following estimate:

$$\frac{\Gamma(T)}{H(T)} \sim \frac{T^3(GT)^2}{T^2/M_{\mathrm{Pl}}} = \left(\frac{T}{M_{\mathrm{Pl}}}\right)^3, \tag{24}$$

where M_{Pl} is the Planck mass, $G = 1/M_{\mathrm{Pl}}^2$ is the gravitational constant, and $H(T)$ is the Hubble parameter when the temperature of the Universe is equal to T. $\Gamma(T) = n\sigma v$ gives the probability of gravitational interaction of particles with the interaction cross section $\sigma \sim G^2T^2$, velocity $v \sim 1$, and number density $n \sim T^3$. The above expression suggests that the interaction rate between GWs and the surrounding matter is less than the Hubble parameter for essentially all temperatures $T < M_{\rm Pl}$. Thus, GWs propagate freely in the Universe and carry unaltered information about the processes in which they were created. As a consequence, cosmological GWs offer a unique tool for studying extreme physics at ultrahigh energies at the very early epochs of the Universe, which cannot be probed by other means. Among other things, the detection of the CGWB offers a probe for New Physics beyond the Standard Model complementing the existing experiments at the Large Hadron Collider at energies up to ~ 14 TeV.

Relic GWs (tensor perturbations of the metric) arise directly from parametric amplification of the primordial quantum fluctuations at the time of the accelerated expansion during the inflationary stage [1, 50]. Nearly flat or (weakly) red GW spectra are a common property of the conventional slow-roll inflation, so the power spectral density can be parametrized as $P_T(f) \sim f^{n_T}$, $n_T = -r/8$, where $r = T/S$ is the ratio of tensor to scalar modes of the primordial cosmological perturbations; $r < 0.032$ at a 95% confidence level obtained from an analysis of the CMB [51]. Assuming that the inflationary spectrum with a constant n_T can be extrapolated over many orders of magnitude down to lower frequencies, the expected amplitude of the CGWB is given by [52][7]

$$\Omega_{\rm GW}(f) \approx 1.5 \times 10^{-16} \left(\frac{r}{0.032}\right) \left(\frac{f}{f_*}\right)^{n_T}, \tag{25}$$

where $f_* \approx 7.7 \times 10^{-17}$ Hz is the frequency related to the CMB scale of $k = 0.05\ \text{Mpc}^{-1}$. It is evident that for $n_T \sim 0$ the predicted amplitude of the standard inflationary CGWB is far below the value derived from recent PTA observations, which corresponds to a GWB energy density of $\Omega_{\rm GW} \sim 10^{-10}$ (see equation (17)).

Another process that may contribute to the generation of the background in the early Universe is phase transitions. As the plasma temperature decreases, the Universe undergoes first- and second-order phase transitions, the former being of particular interest in the context of PTAs. For first-order phase transitions, the average value of the phase of the Higgs field $\langle \phi_T \rangle = 0$ changes abruptly to a state with $\langle \phi_T \rangle \neq 0$, which is favored thermodynamically. It is not possible for such a change in the system to occur in the entire space at the same time. The transition is characterized by the formation of bubbles of the new phase and their subsequent expansion at velocities approaching the speed of light (see [56] for more details on the physics of phase transitions and the early Universe baryogenesis initiated by them). The primary consequence of the expansion of bubbles is the heating of the surrounding plasma, and this process does not result in the generation of GWs. Nevertheless, a fraction of the kinetic energy of the scalar field is transferred to the bulk motion of matter and sound waves. By the end of the phase transition, the bubbles merge with additional energy release. The last two processes (bulk flow and bubble merging) result in the effective generation of GW radiation due to the nonzero stress tensor Π. The shape of the power spectral density of the GWB produced by the bubble collision, when the temperature and density of the Universe are equal to T and $\rho_{\rm tot}$, respectively, is given by

$$\Omega_{\rm GW}(f) \simeq 1.6 \times 10^{-5} \left(\frac{100}{g_*(T)}\right)^{1/3} \left(\frac{H(t)}{\beta}\right) \left(\frac{\Pi}{\rho_{\rm tot}}\right)^2, \tag{26}$$

where g_* is the effective number of relativistic degrees of freedom, and $1/\beta$ is the characteristic timescale of the phase transition. For sound waves, the energy density of the generated GWB is

$$\Omega_{\rm GW}(f) \simeq 1.6 \times 10^{-5} \left(\frac{100}{g_*(T)}\right)^{1/3} \left(\frac{H(t)}{\beta}\right) \left(\frac{\Pi}{\rho_{\rm tot}}\right)^2 \times v_{\rm w} \left(\frac{f}{f_0}\right) \left(\frac{7}{4 + 3(f/f_0)^2}\right)^{7/2}, \tag{27}$$

where $f_0 \simeq 2\sqrt{3}(\beta/v_{\rm w})$, and $v_{\rm w}$ is the bubble expansion velocity. Both these expressions are interpolations of the results of numerical calculations. In addition, the first-order phase transitions instigate a plethora of further processes, consequently resulting in the generation of GWs within the frequency range that PT is sensitive to. Among them are the MHD turbulence of the primordial plasma [57–62] and cosmic strings [63–67], which are topological defects that emit GWs through bursts of cusps, kinks, and kink–kink collisions on the loops.

Another interesting mechanism responsible for the generation of GW radiation relates to scalar curvature perturbations in the early Universe. The magnitude of such scalar perturbations is associated with primordial density inhomogeneities, which are being measured using CMB temperature maps. The latest data from the Planck space telescope [51] suggests that the power spectrum of scalar perturbations $P_\zeta(k)$ measured at scales $k \sim 10^{-4} - 1\ \text{Mpc}^{-1}$ is nearly flat with the amplitude $A_\zeta = 2 \times 10^{-9}$.

In the linear approximation of Einstein's equations, scalar, vector, and tensor modes propagate independently of each other. But, in the second order of the perturbation theory, scalar modes can launch propagating tensor modes (GWs). In particular, for the power-law spectral density of the primordial fluctuations $P_\zeta = A_\zeta^{10\,\rm yr}(k/k_{10\,\rm yr})^{n_s-1}$, the GW energy is

$$\Omega_{\rm GW}\left(f = \frac{kc}{2\pi}\right) \simeq (A_\zeta^{10\,\rm yr})^2 \left(\frac{k}{k_{10\,\rm yr}}\right)^{2(n_s-1)}. \tag{28}$$

Therefore, by probing such a CGWB, PT enables the estimation of scalar curvature perturbations on much smaller scales than typical CMB scales, with the characteristic wave numbers $k \sim 10^6 - 10^8\ \text{Mpc}^{-1}$. Probing inhomogeneities on such scales could help us to determine the number of primordial black holes (PBHs) with characteristic masses of the order of several ten $M_\odot$. Such PBHs are produced from high peaks in the density field when their characteristic size becomes comparable to the size of the cosmological horizon:

$$M(k) \sim 30 M_\odot \left(\frac{10.75}{g_*}\right)^{-1/6} \left(\frac{3 \times 10^5\ \text{Mpc}^{-1}}{k}\right) \tag{29}$$

(g_* is the number of relativistic degrees of freedom).

The results of the interpretation of the signal detected by different PTAs in frameworks of some popular CGWB models, are summarized in Table 2. Different CGWB models can explain the observed PTA signal. These models differ in

[7] With the Hubble constant equal to 67 km s^{-1} Mpc^{-1}.

Table 2. Parameters of different GWB models under the assumption that common red noise detected in PTA data has a cosmological origin.

Model of CGWB	Derived parameters	Literature
Relic GWB from inflation	$\log r = -12.18^{+8.81}_{-7.00}$, $n_T = 2.29^{+0.87}_{-1.11}$ $\log r = -14.06^{+5.82}_{-5.82}$, $n_T = 2.61^{+0.85}_{-0.85}$	[34] [53]
Cosmic strings	$\log G\mu = -10.07^{+0.47}_{-0.36}$(BOS), $-10.63^{+0.24}_{-0.22}$(LRS) [a] $\log G\mu = -10.15^{+0.16}_{-0.16}$(STABLE−C) [b]	[34] [53]
MHD turbulence from QCD phase transition	$\lambda_* \mathcal{H}_* = 1$, $\Omega_* = 0.3$, $T_* = 140$ MeV [c]	[34]
Scalar-induced 2nd-order GWs $\left(P_\zeta = A_\zeta^{10\,\mathrm{yr}}\left(\dfrac{k}{k_{10\,\mathrm{yr}}}\right)^{n_s-1}\right)$ [d]	$\log A_\zeta^{10\,\mathrm{yr}} = -2.9^{+0.42}_{-0.46}$, $n_s = 2.1^{+0.25}_{-0.32}$	[34]
Scalar-induced 2nd-order GWs $(P_\zeta = A_\zeta \delta(k-k_*))$	$\log A_\zeta > -1.7$, $\log(k_*/\mathrm{Mpc}^{-1}) > 7.6$ [e] $\log A_\zeta = -0.69^{+0.47}_{-0.47}$, $\log(k_*/\mathrm{Mpc}^{-1}) = -8.9^{+0.60}_{-0.60}$	[34] [53]
Phase transitions in early Universe	$\log \lambda_* \mathcal{H}_* = -0.81^{+0.36}_{-0.36}$, $\log \alpha_* = 0.3^{+0.44}_{-0.44}$, $\log(T_*/\mathrm{GeV}) = -0.76^{+0.36}_{-0.36}$	[53]

[a] Cosmic string tension in BOS model [54], LRS model [55].
[b] Cosmic string tension in BOS model when only emission from cusps is taken into account.
[c] $\lambda_* \mathcal{H}_*$ is ratio of characteristic length scale of turbulence to comoving Hubble horizon. $\mathcal{H}_*^{-1}$ in QCD epoch with temperature T_* and energy density of MHD turbulence Ω_*.
[d] Power spectrum of primordial scalar perturbations is normalized to $k_{10\,\mathrm{yr}} = 2\pi/10$ yr.
[e] Upper limits at a 95% confidence level.

their spectral properties, thereby potentially enabling us to distinguish one cosmological model from another (and from the astrophysical background). Presently, both the astrophysical and cosmological hypotheses provide equally accurate descriptions of the spectrum of the detected signal [34, 53]. Moreover, based exclusively on the frequency representation of the signal, some of the CGWB models explain the obtained data better than the GWB from SMBHBs [53]. However, this requires a nonstandard set of model parameters in order to significantly boost the production of GW radiation in the early Universe. It should be noted that these conclusions are likely to be subject to further revision as the SNR of the detected signal increases and more complete and realistic aspects of the astrophysical GWB are taken into consideration, such as the effects of the eccentricity of SMBHBs and their interaction with the stars and gas in galaxies.

4. Probing ultralight scalar dark matter using pulsar timing and polarimetry

High-precision observations of MSPs carried out by international collaborations can be used not only to detect the GWB and GWs from individual sources, as was discussed in the previous section. In the pioneering paper by V.A. Rubakov and A. Khmelnitsky [2], it was shown that the presence of ultralight scalar field DM in the Galaxy will induce quasi-monochromatic oscillations in the ToAs of pulses from a pulsar. In addition, the model gives rise to the effect of cosmic birefringence [68, 69], resulting in variations in the orientation of the plane of linearly polarized electromagnetic radiation. The constraints on the ultralight scalar DM obtained from PT and pulsar polarimetry are examined in this section of the review.

4.1 Ultralight pseudoscalar bosons as dark matter

DM continues to be at the cutting edge of fundamental and experimental research in physics, astrophysics, and cosmology [70, 71]. One of the possible candidates for the role of DM is ultralight, weakly interacting pseudoscalar bosons with masses of $m_\mathrm{a} \sim 10^{-22}$ eV. Independent of the DM problem, axions and axion-like particles (ALPs) have also emerged as a consequence of various extensions of the Standard Model. In particular, ALPs were introduced to solve the *CP* violation problem of particle physics [72]. The attractiveness of these particles in cosmology as ultralight DM (ULDM) [73–75] is explained by their rich phenomenology. In particular, such bosons with masses of $\sim 10^{-20}-10^{-23}$ eV could form so-called 'fuzzy' DM [76, 77], which solves some of the problems of cold DM.

The extremely low masses of ALPs combined with characteristic virial velocities of the order of $v \sim 10^{-3}$ make their de-Broglie wavelength $\lambda_\mathrm{dB} = 1/k \sim 1/mv$ ($\geqslant 100$ pc) much larger than the average distance between these particles, i.e., the phase space occupation numbers are huge:

$$\mathcal{N} = \frac{N}{\mathrm{d}^3 x\, \mathrm{d}^3 k} \simeq n\lambda_\mathrm{dB}^3 \sim 10^{95}\left(\frac{\rho_\mathrm{DM}}{0.4\ \mathrm{GeV\ cm^{-3}}}\right)\left(\frac{m_\mathrm{a}}{10^{-22}\ \mathrm{eV}}\right)^{-4}. \tag{30}$$

This allows us to treat their ensembles as purely classical fields (see review [78]).

The classical Bose condensate of ALPs in the Galaxy gives rise to a number of significant phenomenological consequences, which may be tested in astrophysical measurements of pulsars.

(1) An ALP field with boson masses of around $\mathcal{O}(10^{-22})$ eV oscillates coherently with typical frequencies defined by the de-Broglie wavelength $\omega = m_\mathrm{a}$ (accurate to $\Delta\omega/\omega \sim v^2$): $\phi = A\cos(\omega t + \alpha(t))$ [78]. Since the energy–momentum tensor depends quadratically on the field, the time component is $T_{tt} = \rho_\mathrm{DM} = A^2 m_\mathrm{a}^2/2$, and oscillating spatial components are proportional to the gradient of the field: $\rho_\mathrm{DM}^\mathrm{osc} \sim k^2 m_\mathrm{a}^2 = v^2 \rho_\mathrm{DM}$. The angular frequency of these

oscillations is twice the boson mass[8] $\omega^{\rm osc} = 2m_{\rm a}$. Moreover, up to the first order of v/c, only the diagonal components are left:

$$T_{ij} = -\frac{1}{2}\, m_{\rm a}^2 A^2\big(\cos(2m_{\rm a}t) + 2\alpha(t)\big) = p\delta_{ij}\,.$$

The oscillating pressure leads to fluctuations in the gravitational potential, which can be observed by PT and provides independent constraints on the DM density formed by ALPs [2].

(2) The nonrenormalizable coupling of massive scalar ALPs to photons alters the polarization properties of EM waves propagating through an ALP field [68, 69] (known as the birefringence effect). Axion-induced birefringence constraints on the coupling constant between axions and photons $g_{\rm a\gamma}$ were obtained by analyzing linearly polarized light of active galactic nuclei (AGN) [79], from polarimetric observations of protoplanetary disks [80], and by analyzing the linearly polarized component of the CMB [81, 82]. Because of the high degree of linear polarization and extremely stable emission properties, one of the most powerful tools for constraining ALPs is to observe the oscillations in the orientation of the polarization plane of the EM signal from pulsars. For instance, competitive constraints on the coupling constant $g_{\rm a\gamma}$ were obtained with the PPTA data [83, 84].

Below, we consider sequentially the constraints obtained.

4.2 Pulsar timing constraints on ultralight scalar dark matter from integral Sachs–Wolfe effect

The first constraints on the energy density of ultralight scalar DM using the PT method were obtained in [2]. A summary of the key findings of this work is given below. Coherent pressure oscillations of ultralight scalar DM at twice the mass frequency $2m_{\rm a}$ lead to quasi-monochromatic variations of gravitational potentials. Indeed, the metric for small scalar perturbations in the covariant Newtonian gauge is expressed as follows:

$$ds^2 = \big(1 + 2\Phi(x,t)\big)\,dt^2 - \big(1 - 2\Psi(x,t)\big)\,dx^2\,. \tag{31}$$

Newton potentials are time-independent $\Psi_0 = \Phi_0$ and can be found from the tt-components of the Einstein equations,

$$\Delta\Psi_0 = 4\pi G T_{tt} = 4\pi G\rho_{\rm DM}\,,$$

that is, $\Psi_0 \sim G\rho_{\rm DM}/k^2$. Variable gravitational potentials (and similarly $\Phi(x,t)$) are calculated as a trace of spatial ij-components of the Einstein equations,

$$-6\,\frac{\partial^2\Psi}{\partial t^2} + 2\Delta(\Psi - \Phi) = 8\pi G T^j{}_j = 24\pi G p(x,t)\,,$$

and oscillate with the same frequency $\omega = 2m_{\rm a}$ as the pressure $p(x,t)$. In the leading order, $\Psi_s = 0$, and

$$\Psi_c(x) = \frac{1}{2}\,\pi G A^2(x) = \frac{\pi G\rho_{\rm DM}(x)}{m_{\rm a}^2} \tag{32}$$

and $\Psi_c(x) \sim v^2\Psi_0(x)$ (as $k^2 = m_{\rm a}^2 v^2$).

An EM wave with frequency f propagating in varying metric (31) is time-delayed due to the Sachs–Wolfe effect [6]. For an EM wave propagating in the direction n_i, the relationship between the observed frequency f at the position of the observer x at time t and f_0 emitted at x_0, to the leading order (when the Doppler term $n_i v^i \ll 1$ can be neglected), is

$$\frac{\Delta f}{f} = \frac{f - f_0}{f_0} = \Phi(t_0) - \Phi(t) + \int_{t_0}^{t} (\partial_t\Phi - \partial_t\Psi)\,dt'\,, \tag{33}$$

where the first two terms are the gravitational redshift of a photon due to the difference between gravitational potentials Φ at the positions of the observer and the emitter, while the third term represents the integral Sachs–Wolfe effect of an EM wave propagating in the oscillating metric. The integration is performed over the unperturbed trajectory of the photon. Switching to the full derivatives $\partial_t = d/dt - n_i\partial_i$, one gets

$$\frac{f - f_0}{f_0} = \Psi(x,t) - \Psi(x_0,t_0) - \int_{t_0}^{t} n_i\partial_i(\Phi - \Psi)\,dt'. \tag{34}$$

Given that the typical distances to the Galactic sources (pulsars) are usually larger than the characteristic coherence length of the ALP field $D > \lambda_{\rm dB} \sim v/m_{\rm a}$, the expression under the integral is a rapidly oscillating function. As a result, the integral is suppressed by the factor $k/\omega \sim v \ll 1$. The time-dependent redshift of the signal is only determined by the oscillating part of the potential Ψ_c. Therefore, the final expression is given by

$$\frac{\Delta f(t)}{f_0} \approx \Psi(x,t) - \Psi(x_0,t_0) = \Psi_c(x)\cos\big(\omega t + 2\delta(x)\big) - \Psi_c(x_0)\cos\big(\omega(t - D) + 2\delta(x_0)\big)\,. \tag{35}$$

Note that, in this approximation, the effect is independent of the gravitational potential Φ. At $f = \omega/2\pi = m_{\rm a}/\pi$, the amplitude of the effect is determined by the local density of the oscillating scalar DM (see equation (32)):

$$\Psi_c(f) = \frac{\pi G\rho_\phi(x)}{m_{\rm a}^2} = \frac{G\rho_\phi(x)}{\pi f^2} \approx 6.5\times 10^{-18}\left(\frac{m_{\rm a}}{10^{-22}\ \text{eV}}\right)^{-2}\left(\frac{\rho_\phi}{0.4\ \text{GeV cm}^{-3}}\right). \tag{36}$$

The amplitude of the ALP field is determined by the local DM density, which has a stochastic nature. Consequently, the field amplitude both in the vicinity of the pulsar and Earth is randomly distributed around the mean value $\langle\rho_\phi\rangle$: $\rho_\phi(x) = \langle\rho_\phi\rangle\kappa^2(x)$, where $\kappa(x)$ follows the Rayleigh distribution. Using (35), the pulsar timing residuals measured on Earth in $x_{\rm p} = x_0$ for a pulsar located at $x_{\rm e}$ can be expressed as

$$\mathcal{R}(t) = \int_0^t \frac{\Delta f(t')}{f_0}\,dt' = \frac{\Psi_c(x_{\rm e})}{\omega}\sin\big(\omega t + 2\delta(x_{\rm e})\big) - \frac{\Psi_c(x_{\rm p})}{\omega}\sin\big(\omega(t - D) + 2\delta(x_{\rm p})\big)\,, \tag{37}$$

with a typical induced RMS of

$$\sigma_{\rm TOA} = \sqrt{\langle\mathcal{R}^2(t)\rangle} = \frac{1}{2}\,\frac{\Psi_c}{2m_{\rm a}} \approx 0.02\ \text{ns}\left(\frac{m_{\rm a}}{10^{-22}\ \text{eV}}\right)^{-3}\left(\frac{\rho_\phi}{0.4\ \text{GeV cm}^{-3}}\right). \tag{38}$$

The monochromatic signal from ULDM is shown in Fig. 1c.

[8] In natural units, $\hbar = c = k_{\rm B} = 1$ frequency has units of mass (energy). In CGS, the relationship between frequency of oscillation and the ALP mass is $f\,[\text{Hz}] \simeq 2.4\times 10^{-8}(m/10^{-22}\ \text{eV})$.

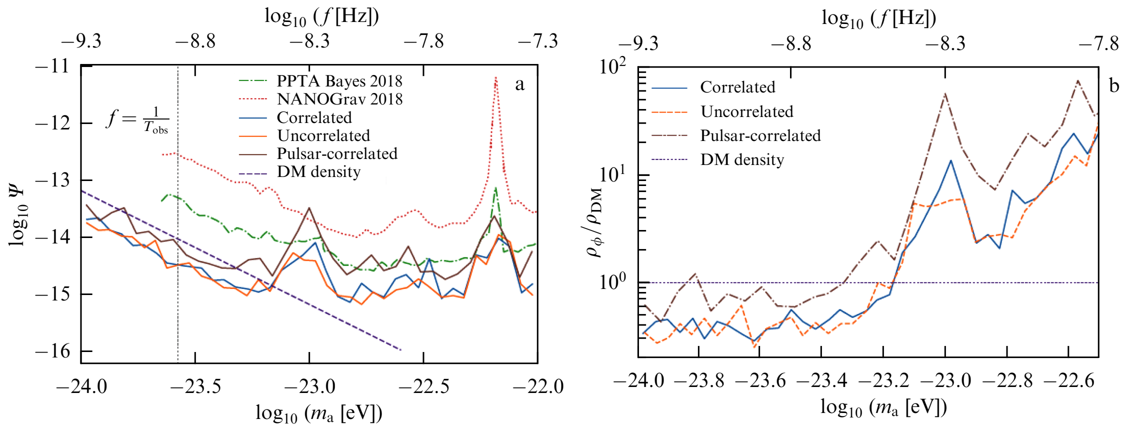

Figure 3. Ninety-five percent upper limits on dimensionless amplitude of ALP field Ψ_c (a) and on ULDM density normalized to local DM density, $\rho_\phi/\rho_{\rm DM}$ (b). Bottom horizontal axis shows ALP mass (eV), while upper horizontal axis is expressed in terms of corresponding frequency $f = \omega/2\pi = m_{\rm a}/\pi \approx 4.8\times10^{-8}\,\mathrm{Hz}(m_{\rm a}/10^{-22}\,\mathrm{eV})$. Solid lines show obtained limits for three different PTA configurations (see text). Dashed-dotted and dotted lines correspond to previously obtained limits in [85, 87], respectively. Dependence of amplitude of oscillation on boson mass (Eqn (36)) is shown by purple dotted line. (Figure taken from [90].)

In the most general case, the phase of the field on Earth $\delta(x_{\rm e}) = \delta_{\rm e}$ (phase of the Earth term) is independent of the phase of the pulsar term $\delta(x_{\rm p}) = \delta_{\rm p}$. The same holds for the stochastic amplitudes $\kappa(x_{\rm e}) = \kappa_{\rm e}$, $\kappa(x_{\rm p}) = \kappa_{\rm p}$. Three different configurations can occur:

(1) Uncorrelated case: the distance between the pulsar and the observer is larger than the coherence length of the field $D > \lambda_{\rm dB}$; phases $\delta_{\rm e}$, $\delta_{\rm p}$ and amplitudes $\kappa_{\rm e}$, $\kappa_{\rm p}$ are independent.

(2) Correlated case: all pulsars and the observer fall within the coherence length $D < \lambda_{\rm dB}$; phases and amplitudes of the field are the same. Moreover, the entire Galacto-centric region is enclosed within the coherence length of the ALP field.

(3) Pulsar-correlated case: the coherence length of the ALP field is larger than the typical Earth-pulsar and pulsar-pulsar distances, but smaller than the Galacto-centric radius. In this case, the DM density estimates obtained from the Galactic rotational curve are averaged over multiple pulsars.

Depending on the configuration, the ULDM signal has a unique signature of correlation between pulsars. As can be seen from equation (37), if $\rho_\phi(x_{\rm e}) \gg \rho_\phi(x_{\rm p})$, the Earth term dominates the pulsar term. In this case, the angular correlation between different pulsars is monopolar, i.e., $\alpha_{ij} = 1$. Oppositely, if $(\rho_\phi(x_{\rm e}) \ll \rho_\phi(x_{\rm p}))$ and all pulsars are located inside different coherence patches, the monopolar correlation is completely lost. In the most general case, the signal from ALPs exhibits a partially monopolar correlation. As shown in [149], the average correlation coefficient α_{ij} is distributed quasi-uniformly between 0 and 1. This is a distinctive feature of the ALP signal, which allows us to distinguish it from, for example, the GWB with quadrupole correlation.

The concept proposed by A. Khmelnitsky and V.A. Rubakov was developed and validated using real data in [53, 85, 86] (NANOGrav) and [87, 88] (PPTA) and using the timing of the millisecond gamma-ray pulsars obtained by Fermi-LAT [89]. The most stringent constraints were inferred in [90] using the EPTA dataset. The density of the ULDM ρ_ϕ was concluded to be less than several tenths of the local DM density (derived independently from kinematic measurements) for the ALP masses $m_{\rm a} \sim [10^{-24}\,\mathrm{eV}, 10^{-23.3}\,\mathrm{eV}]$ (Fig. 3).

The methodology described above can be generalized to the case of vector ULDM [91]. The main difference from the case of scalar DM is a nontrivial correlation pattern between ToAs of different pulsars, and on average a fourfold larger effect than for scalar DM.

4.3 Constraints on ultralight scalar dark matter from pulsar polarimetry

The nonrenormalizable coupling $g_{{\rm a}\gamma}$ between the scalar ϕ and the EM $F_{\mu\nu}$ fields manifests itself in the Lagrangian as follows:

$$\mathcal{L} = -\frac{1}{4}F_{\mu\nu}F^{\mu\nu} + \frac{g_{{\rm a}\gamma}}{4}\,\phi F_{\mu\nu}\tilde{F}^{\mu\nu} + \frac{1}{2}\left(\partial_\mu\phi\partial^\mu\phi - m_{\rm a}^2\phi^2\right), \quad (39)$$

where $\tilde{F}^{\mu\nu}$ is the EM tensor. Note that the constant $g_{{\rm a}\gamma}$ has the dimension of inverse mass. The equations of motion for the Lagrangian (39) are

$$\begin{aligned}&\partial_t^2\mathbf{A} - \nabla^2\mathbf{A} = g_{{\rm a}\gamma}(\partial_t\phi\nabla\times\mathbf{A} + \partial_t\mathbf{A}\times\nabla\phi)\,,\\ &\Box\phi + m_{\rm a}^2\phi = g_{{\rm a}\gamma}\mathbf{EB}\,.\end{aligned} \quad (40)$$

As discussed above, the amplitude of the scalar field ϕ depends on the DM density $\rho_{\rm DM}$:

$$A = \frac{\sqrt{2\rho_{\rm DM}}}{m_{\rm a}} \approx 2.5\times10^{10}\,\mathrm{GeV} \times\left(\frac{\rho_{\rm DM}}{0.4\,\mathrm{GeV\,cm^{-3}}}\right)^{1/2}\left(\frac{10^{-22}\,\mathrm{eV}}{m_{\rm a}}\right). \quad (41)$$

For the considered boson masses and characteristic magnetic fields in the interstellar medium $B \sim \mathcal{O}(\mu\mathrm{G})$ in the second equation (40), the term $g_{{\rm a}\gamma}\mathbf{EB} \ll m_{\rm a}^2\phi$, given typical values of the coupling constant $g_{{\rm a}\gamma} \lesssim 10^{-12}\,\mathrm{GeV^{-1}}$. In other words, one can neglect the backreaction of the EM field on the ALP field ϕ. Then, the temporal evolution of the field is represented by the coherent oscillations with frequency $\omega = m_{\rm a}$:

$$\phi(t,\mathbf{x}) = A(\mathbf{x})\cos\left(m_{\rm a}t + \delta(\mathbf{x})\right). \quad (42)$$

Assuming that $A(\mathbf{x})$ and $\delta(\mathbf{x})$ change on a characteristic timescale significantly longer than the period of ALP oscillation (adiabatic approximation),

$$T_{\mathrm{a}} = \frac{2\pi}{m_{\mathrm{a}}} \approx 4 \times 10^7\ \mathrm{s}\left(\frac{10^{-22}\ \mathrm{eV}}{m_{\mathrm{a}}}\right),$$

and expressing linearly polarized light as a sum of left- and right-handed circularly polarized waves, one gets the dispersive relation for the polarization states [80]:

$$\omega_{\pm}^2 \mp g_{\mathrm{a}\gamma}(\partial_t \phi + \hat{\mathbf{k}}\,\nabla\phi)|k| = 0\,. \tag{43}$$

In a short-wavelength regime $k \gg m_{\mathrm{a}}$, the dispersion relation for the two modes reduces to

$$\omega_{\pm} \simeq k \pm \frac{1}{2}\, g_{\mathrm{a}\gamma}\left(\partial_t\phi + \nabla\phi\,\hat{\mathbf{k}}\right). \tag{44}$$

Therefore, for plane EM waves, the ALP field acts as a birefringent medium. Similarly to classical Faraday rotation, for an EM field propagating from the emitter at x_{p} to the observer at x_{e}, the plane of polarization is rotated by an angle

$$\Delta\theta = \frac{g_{\mathrm{a}\gamma}}{2}\int_{t_{\mathrm{p}}}^{t_{\mathrm{e}}} \frac{\mathrm{d}\phi}{\mathrm{d}t}\,\mathrm{d}t = \frac{g_{\mathrm{a}\gamma}}{2}\left[\phi(t_{\mathrm{e}}, x_{\mathrm{e}}) - \phi(t_{\mathrm{p}}, x_{\mathrm{p}})\right] \equiv \frac{g_{\mathrm{a}\gamma}}{2}\,\Delta\phi\,. \tag{45}$$

However, in contrast to the Faraday rotation, in the adiabatic approximation, the effect from ALPs is independent of the carrier frequency and is only defined by the difference between the field amplitudes ϕ at the pulsar and the observer. Such an approximation holds for timescales and characteristic lengths below $\tau_{\mathrm{c}} = 1/(m_{\mathrm{a}} v^2) \sim 10^6 T_{\mathrm{a}}$ and $l_{\mathrm{c}} \sim \lambda_{\mathrm{dB}} = 1/(m_{\mathrm{a}} v) \sim 60\ \mathrm{pc}\,(10^{-22}\ \mathrm{eV}/m_{\mathrm{a}})$, respectively (Fig. 4).

As in the case of the Sachs–Wolfe integral effect, it is necessary to introduce stochastic amplitudes which are used to describe the inhomogeneity of the ULDM density distribution in the Galaxy. The rotation angle of the polarization plane is written as

$$\Delta\theta(t) = \frac{g_{\mathrm{a}\gamma}}{\sqrt{2}m_{\mathrm{a}}}\Big[\sqrt{\rho_{\mathrm{e}}}\,\kappa_{\mathrm{e}}\cos\left(m_{\mathrm{a}}t + \delta_{\mathrm{e}}\right) - \sqrt{\rho_{\mathrm{p}}}\,\kappa_{\mathrm{p}}\cos\left(m_{\mathrm{a}}(t - T) + \delta_{\mathrm{p}}\right)\Big]\,, \tag{46}$$

where t is the epoch of observation and T is the propagation time from the pulsar to the observer. It is convenient to rewrite this expression in the form

$$\Delta\theta(t) = \Phi_{\mathrm{a}}\cos\left(m_{\mathrm{a}}t + \varphi_{\mathrm{a}}\right), \tag{47}$$

where

$$\Phi_{\mathrm{a}} = \frac{g_{\mathrm{a}\gamma}}{\sqrt{2}\,m_{\mathrm{a}}}\left(\rho_{\mathrm{e}}\kappa_{\mathrm{e}}^2 + \rho_{\mathrm{p}}\kappa_{\mathrm{p}}^2 - 2\sqrt{\rho_{\mathrm{e}}\rho_{\mathrm{p}}}\,\kappa_{\mathrm{e}}\kappa_{\mathrm{p}}\cos\varDelta\right)^{1/2}, \tag{48}$$

with phase $\varDelta = m_{\mathrm{a}}T + \delta_{\mathrm{p}} - \delta_{\mathrm{e}}$, which, due to large uncertainties in the measured distances to pulsars, can be assumed to be uniformly distributed in the interval $[0, 2\pi]$. For typical values $\varDelta = \pi$, $\rho_{\mathrm{e}} = \rho_{\mathrm{p}} = \rho_{\mathrm{DM}}$, and $\kappa_{\mathrm{e}} = \kappa_{\mathrm{p}} = 1$, one gets

$$\Phi_{\mathrm{a}} = g_{\mathrm{a}\gamma}A \approx 0.025\,[\mathrm{rad}]\left(\frac{g_{\mathrm{a}\gamma}}{10^{-12}\ \mathrm{GeV}^{-1}}\right) \times \left(\frac{\rho_{\mathrm{DM}}}{0.4\ \mathrm{GeV\ cm}^{-3}}\right)^{1/2}\left(\frac{10^{-22}\ \mathrm{eV}}{m_{\mathrm{a}}}\right). \tag{49}$$

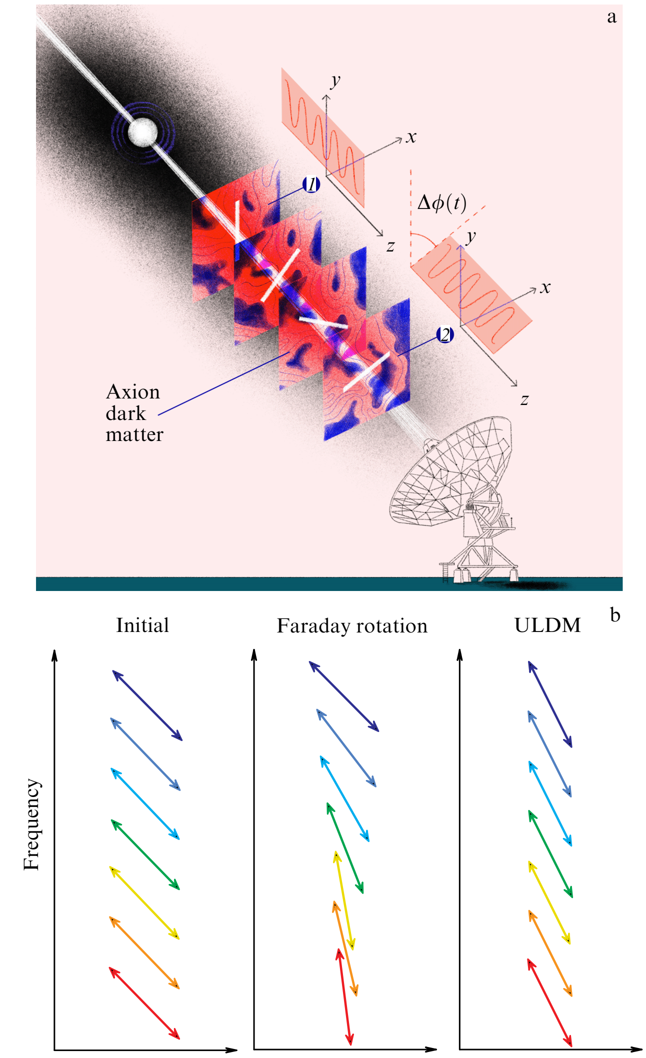

Figure 4. Birefringence of EM wave passing through ALP field. (a) Rotation of plane of linearly polarized pulsar radiation (adopted from [84]). (b) Change in polarization properties of pulsar light due to Faraday rotation and ULDM.

On timescales of a few years, the rotation of the plane of polarization of pulsars typically varies by 1–3° (see Fig. 2 in [84]). The ALP birefringence causes periodic oscillations of the polarization plane of pulsar radiation with typical periods of T_{a}. Searching for such periodic components allows us to impose constraints on the coupling constant $g_{\mathrm{a}\gamma}$ in the range of ALP masses m_{a} [83, 84, 95]. We would like to emphasize the stochastic nature of amplitudes Φ_{a} and phases $\varDelta$, which complicates the search for a periodic component in unevenly sampled pulsar observations. Furthermore, polarimetric measurements can also be biased by a number of other systematic and stochastic effects that are challenging to account for. In particular, the rotation of the plane of polarization of pulsar emission can be attributed to a seasonally varying contribution from the Faraday effect in Earth's ionosphere. More details on the data analysis methods and newly obtained constraints can be found in [149].

The most recent constraints on the coupling constant $g_{\mathrm{a}\gamma}$ as a function of ALP mass m_{a} are presented in Fig. 5 (the solid blue curve adopted from [84]), which were derived from polarimetric analyses of 20 PPTA pulsars and QUIJOTE

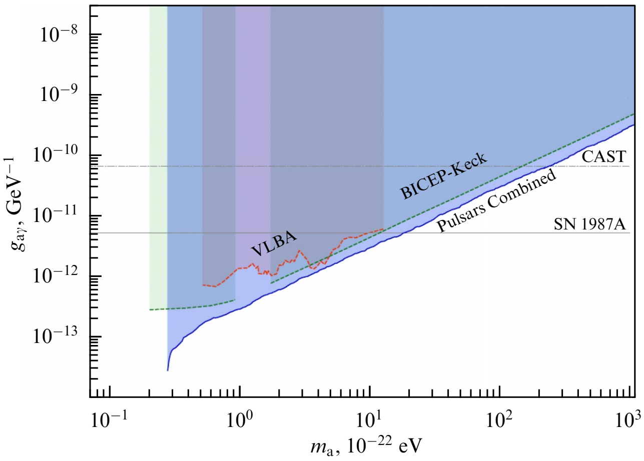

Figure 5. Constraints on axion–photon coupling $g_{a\gamma}$ as a function of boson mass obtained from different astrophysical and laboratory probes: helioscope CAST [92], axion conversion into gamma photons obtained with SN1987A [93], polarimetry study of AGNs using MOJAVE VLBA [79], and CMB polarization with BICEP-Keck [94].

MFI observations of the Crab pulsar used for the PPTA pulsar calibration.

5. Other applications of pulsar timing

5.1 Detection of gravitational wave bursts with memory

The previous sections described the use of PT to detect GWs from SMBHBs at the stage preceding the merger, where the increase in the amplitude and frequency of the signal is relatively slow, i.e., we dealt with quasi-harmonic oscillations. Other types of GW signals also exist. First, at the moment of the merger, there is a short burst with a sharp increase in frequency and amplitude of the signal lasting several ten to hundreds of orbital periods. This type of signal from mergers of stellar mass BHs is detected by LVK laser interferometers.

Second, in so-called 'GWs with memory,' the signal after a GW burst tends to some asymptotic nonzero value [96, 97]. This kind of signal arises if, during the GW generation, there is a permanent change in the value of derivatives of the multipole moments describing the system, which happens if the components of the system before and/or after the GW burst are not gravitationally bound. Initially, the effect was considered for hyperbolic passages of massive bodies with subsequent escape to infinity and for an explosion of supernovae with asymmetric mass ejection. The amplitude of the arising GWs at distance r from the source can be roughly estimated as

$$h_{\mathrm{mem}}(r) \sim \frac{r_{\mathrm{g}}}{r}\left(\frac{v}{c}\right)^2 , \qquad (50)$$

where r_{g} and v are the gravitational radius and velocity corresponding to the nonspherically ejected mass. Obviously, the effect is maximal at the velocity $v = c$, i.e., when the energy is released in the form of photons or GWs.

A significant fraction of the rest mass of merging BHs, up to 10%, is carried away by asymmetrically radiated GWs [98], and a GW burst with memory (BWM), the so-called Christodoulou effect [99–101], arises naturally. The amplitude of the BWM for two identical SMBHs with masses m is given by the following expression:

$$h_{\mathrm{mem}}(r) = 5 \times 10^{-16}\left(\frac{m}{10^8\, M_{\odot}}\right)\left(\frac{1\ \mathrm{Gpc}}{r}\right) . \qquad (51)$$

The effect of BWM on pulsar observations was first studied in [102–104]. The presence of a constant offset in the metric leads to a linear growth in the residuals starting from the moment of the outburst. It should be noted that a BWM signal mimics the effect of incorrectly determined rotational parameters of the pulsar spin frequency and its first derivative, which leads to a bias in the obtained values after fitting for the timing model. An example of emerging residuals can be seen in Fig. 1d.

As can be seen from this example, the amplitude of the perturbed residuals is quite small, even in the case of a merger of relatively close and massive SMBHBs, so it is hardly possible to detect a BWM in observations of a single pulsar. Fortunately, BWMs, like ordinary GWs, cause a correlated response in an array of pulsars, so the observation of a large number of MSPs can significantly increase the sensitivity. In [103], we obtained an estimate of the SNR for detecting a BWM signal with the amplitude h_{mem}:

$$\mathrm{SNR} \sim 1.5\left(\frac{h_{\mathrm{mem}}}{10^{-15}}\right)\left(\frac{N_t}{250}\right)^{1/2}\left(\frac{N_{\mathrm{psr}}}{20}\right)^{1/2}\left(\frac{T_{\mathrm{obs}}}{10\ \mathrm{yr}}\right)\left(\frac{100\ \mathrm{ns}}{\sigma_n}\right) , \qquad (52)$$

where N_{psr} is the total number of observed pulsars, N_t is the number of observations of individual pulsars, T_{obs} is the total duration of observations, and σ_n is the RMS of the ToA residuals. The characteristic values of the parameters are taken for future observations of pulsars with the Square Kilometer Array (SKA) telescope. Assuming the theoretically expected distribution of merging SMBHBs, we can estimate the expected number of detections at the desired SNR level:

$$N \simeq 10^{-1}\left(\frac{N_t}{250}\right)\left(\frac{N_{\mathrm{psr}}}{20}\right)\left(\frac{T_{\mathrm{obs}}}{10\ \mathrm{yr}}\right)^3\left(\frac{100\ \mathrm{ns}}{\sigma_n}\right)^2\left(\frac{3}{\mathrm{SNR}}\right)^2 . \qquad (53)$$

BWMs are also searched for in the currently available PTA datasets [105, 106]. The best constraints were set by analyzing data from the 12.5-year dataset of NANOGrav. There is a weak indication of a BWM presence, but it may arise from the noise artifacts of individual pulsars in the PTA. More conservative estimates give a 95% upper limit on the burst amplitude of $h_{\mathrm{mem}} < 3.3 \times 10^{-14}$.

It should be noted that a similar pattern in the residuals can be caused by the intersection of a LoS and a pulsar by a topological defect, a cosmic string, as a result of the Kaiser–Stebbins effect [107]. An important difference is that the effect now acts only on the individual pulsar, so no correlated signal appears[9] in the entire PTA. In this case, the gain is only possible because of the increased number of potential targets. On the other hand, the amplitude of the effect depends only on the tension of the cosmic string and can be much larger than $\mathcal{O}(10\ \mathrm{ns})$. In [108], it was shown that pulsar observations

[9] It should be emphasized that, in this case, we are talking about the signal caused by an individual string on the LoS, not the GWB produced by the string ensemble discussed in Section 3.4.

allow us to significantly constrain the population of cosmic string loops in the Galaxy for tensions $G\mu/c^2 > 10^{-14}$.

5.2 Search for alternative modes of gravitational wave polarization

In the previous part of the paper, we discussed methods of searching for GWs in the framework of GR. In this theory of gravity, the GWs are transverse waves and have two states of polarization. The situation can be more complicated in alternative theories of gravity, where additional polarization states can arise, since in metric theories the maximum possible number of states is six [109]. Possible additional polarizations will change the response of the GW detectors, which in turn will provide constraints on these alternative theories [110].

The first application of this idea to pulsar timing was made in [111]. It was shown that additional polarization states cause significant modifications to the shape of the HD curve (see Section 2.2). It was estimated that the level of sensitivity required to detect conventional GWs would also be sufficient to detect one of the additional states — the scalar transverse mode — and this level could be achieved by observing 40 pulsars every two weeks for five years at an accuracy level of 100 ns. More detailed calculations were made in [112, 113], where it was shown that the sensitivity of PTAs to nonstandard modes is much higher than to ordinary ones, especially when correlating signals from pulsars located at a small angular distance from each other in the sky.

An analysis of the observations was used to place constraints on the contribution of nonstandard modes: the amplitude of the strongest scalar transverse mode does not exceed 1.4×10^{-15} [114, 115]. The analysis of 15 years of NANOGrav observations, in which the detection of GWs is statistically significant (see Section 3.1 above), confirms these results [116].

5.3 Constraints on graviton mass and GW propagation velocity

In a similar way, one can obtain constraints on the graviton mass, which can be different from zero in many alternative theories [117, 118]. A nonzero graviton mass would lead to a modification of the HD curve due to two effects. First, the nonzero mass and the corresponding velocity difference between EM waves and GWs reduces the level of correlation [119]. Second, in models with massive gravitons, additional polarization modes are likely to arise and that would affect the shape of the curve as was described earlier in Section 5.2 [120]. The latest NANOGrav observations limit the graviton mass from above: $m_{\mathrm{g}} < 8.2 \times 10^{-24}\ \mathrm{eV}/c^2$.

Obviously, questions concerning the graviton mass and the propagation velocity of GWs are closely related. With a nonzero graviton mass, the propagation velocity of GWs v_{g} is less than the speed of light c. Simultaneous observations of GW and EM signals from the GW170817 event [121] have placed very strong constraints on the difference between the their propagation velocities,

$$-3 \times 10^{-15} < \frac{v_{\mathrm{g}} - c}{c} < 7 \times 10^{-16}\,.$$

However, these constraints were derived for $\mathcal{O}(10^2)$ Hz GW frequency and in many models may depend on the GW frequency, so that constraints may be much weaker at nHz frequencies which PTAs are sensitive to [122]. Pulsar observations can also limit the superluminal propagation of GWs. In such regimes, the so-called surfing effect will occur and the amplitude of GW-induced residuals will grow resonantly [123]. The absence of the resonant term in the observed residuals allows us to limit the magnitude of the velocity difference $\epsilon \equiv (v_{\mathrm{g}} - c)/c < 10^{-2}$.

In addition, the non-observation of excess noise in the residuals rules out the possibility that massive gravitons may contribute significantly to DM [124]. This theoretically attractive idea was proposed in [125]. A comprehensive review of possible tests of alternative theories of gravity using GW detectors is presented in [126].

5.4 Study of mass distribution in the Galaxy and search for compact objects

Nontrivial effects in PT arise when the signal propagates from the source to the observer in nonstationary space–time. If there is a moving gravitating mass near the propagation path, then the space–time metric is nonstationary. As a result, a nontrivial pattern in the PT residual appears. The delay Δt in the signal propagation in the vicinity of a gravitating body is known as the Shapiro delay and in the simplest case of a point mass is described as follows [127, 128]:

$$\Delta t = \frac{2GM}{c^3} \ln\left(\frac{4r_{\mathrm{lo}}r_{\mathrm{ls}}}{\rho^2}\right), \tag{54}$$

where M is the mass of the compact object, $r_{\mathrm{lo}}, r_{\mathrm{ls}}$ are distances from the object to the observer and to the pulsar, respectively, and ρ is the impact parameter, the distance of the closest approach between the signal and the gravitating body. The delay consists of two parts: first, the path length increases due to the light bending in the gravitational field of the massive body; second, there is an additional time delay due to signal propagation in this field.

The Shapiro delay is taken into account in pulsar observations when the gravitating object is a companion of the pulsar in a binary system or is in the Solar system. In these cases, it is possible to include the effect in the pulsar timing model with subsequent refinement of the parameters of the object. If the effect occurs 'on the way,' though, it cannot be absorbed by the pulsar timing model, and characteristic features in the pulsar timing residual appear [128, 129]. This effect is similar to that of gravitational lensing, and in a similar way PT allows us to study the distribution of gravitating masses in the Galaxy, including its central regions and beyond, where the usual search for gravitational lensing is difficult [128–131].

Artifacts in the PT residuals also occur when the gravitating object is extended, and this can be used to search for light mini-halos of DM and to set the corresponding constraints on the mass spectrum of perturbations on small scales [132]. The Solar system itself can also act as a detector: the close passage of a gravitating mass and the resulting shift of the system's barycenter will cause a characteristic response in the TOA residuals of the observed pulsars. This response will exhibit a dipole correlation for different pulsar pairs in the PTA.[10] The use of this Doppler effect to search for PBHs with masses of about 10^{25} g ($10^{-8} M_{\odot}$) was proposed in [133].

Further potential applications of the PT method were studied in [134–137]. It was shown that the Doppler counterpart of the induced signal makes a major contribution to the potential detection, as it is correlated between the pulsars.

[10] A similar effect will be observed when a body passes close to the pulsar, but obviously there will be no correlation in the whole network.

Future SKA observations of 200 pulsars observed over 20 years at an accuracy level of 50 ns can significantly constrain the abundance of PBHs and mini-halos over a wide mass range of $10^{-8}-10^{2}M_{\odot}$, which is larger than that probed by the gravitational microlensing method. The analysis in [137] was applied to 15 years of NANOGrav observations [28]. The obtained constraints on PBH abundance and their contribution to the total DM density are so far much weaker than theoretically possible estimates, $f \equiv \Omega_{\rm PBH}/\Omega_{\rm DM} \sim \mathcal{O}(10^2) \gg 1$.

The weakness of the obtained constraints is related both to much more modest capabilities of NANOGrav compared to the future parameters of the SKA PTA, and to the idealization of the noise characteristics of pulsars in the theoretical estimates. It was assumed that the residuals behave like white noise, while many real pulsars have a significant contribution from intrinsic 'red' noise (arising due to the rotation instability of pulsars), which substantially reduces the sensitivity of the PTA to the considered effects.

6. Prospects of pulsar timing method

By now, the direct detection of GWs has only been achieved at high frequencies by LIGO/Virgo/KAGRA ground-based gravitational interferometers. PT uniquely complements these measurements in the nHz range. Recent evidence suggests that a detection of GWs at a high level of significance awaits us in the near future. International pulsar collaborations are undertaking the necessary steps to reach this objective as soon as possible. Further progress in the field of PT is related to three key aspects.

Increasing the significance of detection. Combining the data sets of individual regional PTAs within the framework of the IPTA is the most natural step toward increasing the SNR of the detected signal. The combination will inevitably lead to both more complete and regular coverage of the celestial sphere by pulsars and an increase in their total number, which will enable a better measurement of the HD curve. It is expected that, as a result of data combination, which is a very labor-intensive process requiring huge human resources, the sensitivity of the final PTA will be doubled and the GW signal will be reliably detected with a significance of higher than 5σ.

An increase in the detection significance can also be achieved by extending the total observation time T. However, it is worth noting that an increase in the SNR slows down from $T^{13/3}$ to $T^{1/2}$ when the transition from the weak signal mode to the detection mode takes place. Moreover, as the timespan of observations increases, the contribution of stochastic processes such as the pulsar's intrinsic noise and the turbulence of the interstellar medium, both of which complicate the search for the GW signal, becomes significant. An alternative method to increase the SNR is to use more sensitive radio telescopes for regular monitoring of pulsars, which will improve the timing accuracy and, consequently, reduce the contribution of the instrumental white noise. For example, the PTA based on only 4–5 years of data collected with the MeerKAT [138] and FAST [139] radio telescopes has a sensitivity comparable to those achieved by historical PTA collaborations over the time span of decades. SKA [140] and DSA-2000 (Deep Synoptic Array [141]), which are expected to be operational in the next decade, plan to launch extensive pulsar programs that will unprecedentedly increase the sensitivity of future PTAs to various kinds of astrophysical signals.

Optimization of pulsar networks and algorithms used. One of the main challenges in this field of astrophysics is a high computational complexity and the challenge of Big Data. In addition to big data volumes, one needs to solve a multiparameter optimization problem when searching for a GW signal (at present, the number of free parameters of the problem amounts to ~ 300). Therefore, studying various methods of optimization and increasing the speed of computation are two of the priority directions in the PT field. In particular, advanced Markov chain Monte Carlo schemes have been developed [142], and machine learning methods have been introduced into the PT data analysis schemes [143]. The launch of DSA-2000 and SKA will further increase the volume of processed data due to newly discovered pulsars, which once again emphasizes the relevance of the optimization problem.

Identifying the nature of the signal. To date, it is impossible to determine conclusively the nature of the detected correlated stochastic signal in the residuals. We may be dealing with the cosmological GWB generated in the early Universe, or with astrophysical GWs from the entire population of SMBHBs, or even from a single bright source. There is also a possibility that the detected signal is a combination of astrophysical and cosmological backgrounds. In [34, 53], attempts were made to identify the signal based solely on its spectral characteristics. But as was shown in the previous sections, the shapes of the spectra of the cosmological and astrophysical backgrounds can vary greatly, depending on the underlying assumptions. In particular, the power spectral density of the astrophysical background $S_h(f)$, when taking into account the eccentricities of merging binaries and the finiteness of the number of sources, strictly speaking, is not described by a power law. Thus, considering only spectral characteristics, two types of GWBs are indistinguishable, and the problem of signal identification becomes degenerate.

However, the degeneracy can be removed by including additional observables in the analysis and using nonstandard statistical characteristics of the signal (see, e.g., [32]). One such characteristic is the spatial anisotropy of the GW signal. The astrophysical GW background, which is an incoherent sum from individual SMBHBs, is expected to have a high degree of anisotropy, especially at high frequencies, where individual sources will dominate the mean background. As shown in [144], some astrophysical models predict a significant level of anisotropy, already exceeding the current upper estimates at $C_1/C_0 \leqslant 0.2$ derived in [145]. The sensitivity to anisotropy of the GWB will continue to increase with the addition of new pulsars to a PTA and with decreasing standard RMS $\sigma_{\rm TOA}$ of the residuals as $\sqrt{N_{\rm psr}/\sigma_{\rm TOA}}$ [146, 147]. The lack of anisotropy in the data obtained with the latest pulsar observational programs will enable us to strongly constrain the parameter space of the merging SMBHB models or exclude the astrophysical nature of the signal. However, it is worth noting that a number of effects, such as the cosmological variance of the HD curve, which has similar observational manifestations, can strongly weaken sensitivity to anisotropy probes [148].

Note added in proof

After this review was accepted for publication, improved constraints on the axion–photon coupling were reported from the pulsar polarimetry [149, 150].

Acknowledgements

The work of K.P. and M.P. was supported by grant 075-15-2024-541 from the Ministry of Education and Science of the Russian Federation under the program for financing major scientific projects of the national project Science. The work of NP was supported by Deutsche Forschungsgemeinschaft (DFG, German Research Society) — project number PO 2758/1–1, under the Walter-Benjamin Fellowship.

References

1. Rubakov V A, Sazhin M V, Veryaskin A V *Phys. Lett. B* **115** (3) 189 (1982)
2. Khmelnitsky A, Rubakov V *J. Cosmol. Astropart. Phys.* **2014** (2) 019 (2014)
3. Sazhin M V *Sov. Astron.* **22** 36 (1978); *Astron. Zh.* **55** 65 (1978)
4. Detweiler S *Astrophys. J.* **234** 1100 (1979)
5. Estabrook F B, Wahlquist H D *Gen. Relat. Gravit.* **6** 439 (1975)
6. Sachs R K, Wolfe A M *Astrophys. J.* **147** 73 (1967)
7. Starobinskii A A *Sov. Astron. Lett.* **11** 133 (1985); *Pis'ma Astron. Zh.* **11** 323 (1985)
8. Jenet F A et al. *Astrophys. J.* **606** 799 (2004)
9. Wen Z L et al. *Astrophys. J.* **730** (1) 29 (2011)
10. Burke-Spolaor S et al. *Astron. Astrophys. Rev.* **27** (1) 5 (2019)
11. Lorimer D R, Kramer M *Handbook of Pulsar Astronomy* (Cambridge: Cambridge Univ. Press, 2012)
12. Beskin V S *Phys. Usp.* **61** 353 (2018); *Usp. Fiz. Nauk* **188** 377 (2018)
13. Backer D C, Hellings R W *Annu. Rev. Astron. Astrophys.* **24** 537 (1986)
14. Doroshenko O V, Kopeikin S M *Sov. Astron.* **34** 496 (1990); *Astron. Zh.* **67** 986 (1990)
15. Vallisneri M et al. *Astrophys. J.* **893** (2) 112 (2020)
16. Hobbs G B, Edwards R T, Manchester R N *Mon. Not. R. Astron. Soc.* **369** (2) 655 (2006)
17. Edwards R T, Hobbs G B, Manchester R N *Mon. Not. R. Astron. Soc.* **372** (4) 1549 (2006)
18. Hellings R W, Downs G S *Astrophys. J.* **265** L39 (1983)
19. Bernardo R C, Ng K-W, arXiv:2409.07955
20. Corbin V, Cornish N J, arXiv:1008.1782
21. Allen B, Romano J D *Phys. Rev. D* **108** 043026 (2023)
22. Bernardo R C, Ng K-W *J. Cosmol. Astropart. Phys.* **2022** (11) 046 (2022)
23. Allen B *Phys. Rev. D* **107** 043018 (2023)
24. Thrane E, Romano J D *Phys. Rev. D* **88** 124032 (2013)
25. Siemens X et al. *Class. Quantum Grav.* **30** 224015 (2013)
26. Verbiest J P W et al. *Mon. Not. R. Astron. Soc.* **458** 1267 (2016)
27. Babak S et al. *Phys. Rev. D* **110** 063022 (2024)
28. Agazie G et al. *Astrophys. J. Lett.* **951** (1) L8 (2023)
29. Antoniadis J et al. (EPTA Collab. and InPTA Collab.) *Astron. Astrophys.* **678** A50 (2023)
30. Reardon D J et al. *Astrophys. J. Lett.* **951** (1) L6 (2023)
31. Xu H et al. *Res. Astron. Astrophys.* **23** 075024 (2023)
32. Romano J D, Cornish N J *Living Rev. Relativ.* **20** (1) 2 (2017)
33. Agazie G et al. *Astrophys. J. Lett.* **952** (2) L37 (2023)
34. Antoniadis J et al. (EPTA Collab. and InPTA Collab.) *Astron. Astrophys.* **685** A94 (2024)
35. Volonteri M, Haardt F, Madau P *Astrophys. J.* **582** 559 (2003)
36. Babak S, Sesana A *Phys. Rev. D* **85** 044034 (2012)
37. Antoniadis J et al. (EPTA Collab. and InPTA Collab.) *Astron. Astrophys.* **690** A118 (2024)
38. Agazie G et al. *Astrophys. J. Lett.* **951** (2) L50 (2023)
39. De Rosa A et al. *New Astron. Rev.* **86** 101525 (2019)
40. Dotti M, Sesana A, Decarli R *Adv. Astron.* **2012** 940568 (2012)
41. Rosado P A, Sesana A, Gair J *Mon. Not. R. Astron. Soc.* **451** 2417 (2015)
42. Phinney E S, astro-ph/0108028
43. Sato-Polito G, Zaldarriaga M, Quataert E, arXiv:2312.06756
44. Izquierdo-Villalba D et al. *Astron. Astrophys.* **686** A183 (2024)
45. Bécsy B et al. *Astrophys. J.* **959** (1) 9 (2023)
46. Grishchuk L P et al. *Phys. Usp.* **44** 1 (2001); *Usp. Fiz. Nauk* **171** 3 (2001)
47. Grishchuk L P *Phys. Usp.* **48** 1235 (2005); *Usp. Fiz. Nauk* **175** 1289 (2005)
48. Guzzetti M C et al. *Riv. Nuovo Cimento* **39** 399 (2016) http://dx.doi.org/10.1393/ncr/i2016-10127-1
49. Caprini C, Figueroa D G *Class. Quantum Grav.* **35** 163001 (2018)
50. Grishchuk L P *Sov. Phys. JETP* **40** 409 (1975); *Zh. Eksp. Teor. Fiz.* **67** 825 (1975)
51. Akrami Y et al. (Planck Collab.) *Astron. Astrophys.* **641** A10 (2020)
52. Lasky P D et al. *Phys. Rev. X* **6** 011035 (2016)
53. Afzal A et al. *Astrophys. J. Lett.* **951** (1) L11 (2023)
54. Blanco-Pillado J J, Olum K D, Shlaer B *Phys. Rev. D* **92** 063528 (2015)
55. Lorenz L, Ringeval C, Sakellariadou M *J. Cosmol. Astropart. Phys.* **2010** (10) 003 (2010)
56. Konstandin T *Phys. Usp.* **56** 747 (2013); *Usp. Fiz. Nauk* **183** 785 (2013)
57. Kamionkowski M, Kosowsky A, Turner M S *Phys. Rev. D* **49** 2837 (1994)
58. Kosowsky A, Mack A, Kahniashvili T *Phys. Rev. D* **66** 024030 (2002)
59. Dolgov A D, Grasso D, Nicolis A *Phys. Rev. D* **66** 103505 (2002)
60. Caprini C, Durrer R *Phys. Rev. D* **74** 063521 (2006)
61. Gogoberidze G, Kahniashvili T, Kosowsky A *Phys. Rev. D* **76** 083002 (2007)
62. Caprini C, Durrer R, Servant G *J. Cosmol. Astropart. Phys.* **2009** (12) 024 (2009)
63. Kibble T W B *J. Phys. A* **9** 1387 (1976)
64. Hindmarsh M B, Kibble T W B *Rep. Prog. Phys.* **58** 477 (1995)
65. Siemens X, Mandic V, Creighton J *Phys. Rev. Lett.* **98** 111101 (2007)
66. Sanidas S A, Battye R A, Stappers B W *Phys. Rev. D* **85** 122003 (2012)
67. Quelquejay Leclere H et al. *Phys. Rev. D* **108** 123527 (2023)
68. Carroll S M, Field G B, Jackiw R *Phys. Rev. D* **41** 1231 (1990)
69. Harari D, Sikivie P *Phys. Lett. B* **289** 67 (1992)
70. Zasov A V et al. *Phys. Usp.* **60** 3 (2017); *Usp. Fiz. Nauk* **187** 3 (2017)
71. Bertone G, Hooper D *Rev. Mod. Phys.* **90** 045002 (2018)
72. Jaeckel J, Ringwald A *Annu. Rev. Nucl. Part. Sci.* **60** 405 (2010)
73. Preskill J, Wise M B, Wilczek F *Phys. Lett. B* **120** (1–3) 127 (1983)
74. Abbott L F, Sikivie P *Phys. Lett. B* **120** (1–3) 133 (1983)
75. Dine M, Fischler W *Phys. Lett. B* **120** (1–3) 137 (1983)
76. Hu W, Barkana R, Gruzinov A *Phys. Rev. Lett.* **85** 1158 (2000)
77. Hui L et al. *Phys. Rev. D* **95** 043541 (2017)
78. Hui L *Annu. Rev. Astron. Astrophys.* **59** 247 (2021)
79. Ivanov M M et al. *J. Cosmol. Astropart. Phys.* **2019** (2) 059 (2019)
80. Fujita T, Tazaki R, Toma K *Phys. Rev. Lett.* **122** 191101 (2019)
81. Fedderke M A, Graham P W, Rajendran S *Phys. Rev. D* **100** 015040 (2019)
82. Sigl G, Trivedi P, arXiv:1811.07873
83. Caputo A et al. *Phys. Rev. D* **100** 063515 (2019)
84. Castillo A et al. *J. Cosmol. Astropart. Phys.* **2022** (6) 014 (2022)
85. Porayko N K, Postnov K A *Phys. Rev. D* **90** 062008 (2014)
86. Kato R, Soda J *J. Cosmol. Astropart. Phys.* **2020** (9) 036 (2020)
87. Porayko N K et al. (PPTA Collab.) *Phys. Rev. D* **98** 102002 (2018)
88. Xue X et al. *Phys. Rev. Research* **4** (1) L012022 (2022)
89. Xia Z-Q et al. *Phys. Rev. D* **107** L121302 (2023)
90. Smarra C et al. *Phys. Rev. Lett.* **131** 171001 (2023)
91. Nomura K, Ito A, Soda J *Eur. Phys. J. C* **80** 419 (2020)
92. Anastassopoulos V et al. (CAST Collab.) *Nature Phys.* **13** 584 (2017)
93. Payez A et al. *J. Cosmol. Astropart. Phys.* **2015** (2) 006 (2015)
94. Ade P A R et al. (BICEP/Keck Collab.) *Phys. Rev. D* **105** 022006 (2022)
95. Liu T, Smoot G, Zhao Y *Phys. Rev. D* **101** 063012 (2020)
96. Zel'dovich Ya B, Polnarev A G *Sov. Astron.* **18** 17 (1974); *Astron. Zh.* **51** 30 (1974)
97. Braginsky V B, Thorne K S *Nature* **327** 123 (1987)
98. Reisswig C et al. *Phys. Rev. D* **80** 124026 (2009)
99. Payne P N *Phys. Rev. D* **28** 1894 (1983)
100. Christodoulou D *Phys. Rev. Lett.* **67** 1486 (1991)
101. Favata M *Class. Quantum Grav.* **27** 084036 (2010)
102. Seto N *Mon. Not. R. Astron. Soc.* **400** (1) L38 (2009)
103. Pshirkov M S, Baskaran D, Postnov K A *Mon. Not. R. Astron. Soc.* **402** 417 (2010)
104. van Haasteren R, Levin Y *Mon. Not. R. Astron. Soc.* **401** 2372 (2010)

105. Wang J B et al. *Mon. Not. R. Astron. Soc.* **446** 1657 (2015)
106. Agazie G et al. *Astrophys. J.* **963** (1) 61 (2024)
107. Kaiser N, Stebbins A *Nature* **310** 391 (1984)
108. Pshirkov M S, Tuntsov A V *Phys. Rev. D* **81** 083519 (2010)
109. Alves M E S, Miranda O D, de Araujo J C N *Class. Quantum Grav.* **27** 145010 (2010)
110. Eardley D M et al. *Phys. Rev. Lett.* **30** 884 (1973)
111. Lee K J, Jenet F A, Price R H *Astrophys. J.* **685** 1304 (2008)
112. Chamberlin S J, Siemens X *Phys. Rev. D* **85** 082001 (2012)
113. Gair J R, Romano J D, Taylor S R *Phys. Rev. D* **92** 102003 (2015)
114. Arzoumanian Z et al. *Astrophys. J. Lett.* **923** (2) L22 (2021)
115. Wu Y-M, Chen Z-C, Huang Q-G *Astrophys. J.* **925** (1) 37 (2022)
116. Agazie G et al. *Astrophys. J. Lett.* **964** (1) L14 (2024)
117. Rubakov V A, Tinyakov P G *Phys. Usp.* **51** 759 (2008); *Usp. Fiz. Nauk* **178** 785 (2008)
118. de Rham C *Living Rev. Relativ.* **17** (1) 7 (2014)
119. Lee K et al. *Astrophys. J.* **722** 1589 (2010)
120. Liang Q, Trodden M *Phys. Rev. D* **104** 084052 (2021)
121. Abbott B P et al. *Astrophys. J. Lett.* **848** (2) L13 (2017)
122. Qin W, Boddy K K, Kamionkowski M *Phys. Rev. D* **103** 024045 (2021)
123. Baskaran D et al. *Phys. Rev. D* **78** 044018 (2008)
124. Pshirkov M, Tuntsov A, Postnov K A *Phys. Rev. Lett.* **101** 261101 (2008)
125. Dubovsky S L, Tinyakov P G, Tkachev I I *Phys. Rev. Lett.* **94** 181102 (2005)
126. Yunes N, Siemens X, Yagi K, arXiv:2408.05240
127. Shapiro I I *Phys. Rev. Lett.* **13** 789 (1964)
128. Pshirkov M S, Sazhin M V, Ilyasov Yu P *Astron. Lett.* **34** (6) 397 (2008); *Pis'ma Astron. Zh.* **34** (6) 437 (2008)
129. Larchenkova T I, Doroshenko O V *Astron. Astrophys.* **297** 607 (1995)
130. Wex N, Gil J, Sendyk M *Astron. Astrophys.* **311** 746 (1996)
131. Hosokawa M, Ohnishi K, Fukushima T *Astron. Astrophys.* **351** 393 (1999)
132. Siegel E R, Hertzberg M P, Fry J N *Mon. Not. R. Astron. Soc.* **382** (2) 879 (2007)
133. Seto N, Cooray A *Astrophys. J.* **659** (1) L33 (2007)
134. Baghram S, Afshordi N, Zurek K M *Phys. Rev. D* **84** 043511 (2011)
135. Dror J A et al. *Phys. Rev. D* **100** 023003 (2019)
136. Ramani H, Trickle T, Zurek K M *J. Cosmol. Astropart. Phys.* **2020** (12) 033 (2020)
137. Lee V S H et al. *J. Cosmol. Astropart. Phys.* **2021** (08) 025 (2021)
138. Bailes M et al. *Publ. Astron. Soc. Australia* **37** e028 (2020)
139. Nan R, Li D *IOP Conf. Ser. Mater. Sci. Eng.* **44** 012022 (2013) https://doi.org/10.1088/1757-899X/44/1/012022
140. Janssen G et al., in *Advancing Astrophysics with the Square Kilometre Array, AASKA14, June 8–13, 2014, Giardini Naxos, Italy*; *PoS* **AASKA14** 37 (2015) https://doi.org/10.22323/1.215.0037
141. Hallinan G et al. *Bull. Am. Astron. Soc.* **51** 255 (2019)
142. Laal N et al., arXiv:2410.11944
143. Shih D et al. *Phys. Rev. Lett.* **133** 011402 (2024)
144. Gardiner E C et al. *Astrophys. J.* **965** (2) 164 (2024)
145. Agazie G et al. *Astrophys. J. Lett.* **956** (1) L3 (2023)
146. Depta P F et al., arXiv:2407.14460
147. Pol N, Taylor S R, Romano J D *Astrophys. J.* **940** (2) 173 (2022)
148. Konstandin T et al., arXiv:2408.07741
149. Porayko et al., arXiv:2412.02232
150. Xue X et al., arXiv:2412.02229